Alma Mater Studiorum - Università di Bologna

Dipartimento di Fisica e Astronomia
Corso di Laurea in Astrofisica e Cosmologia

Rest frame optical properties of Lyman-alpha emitters from the HETDEX Survey

Tesi di Laurea Magistrale

Candidato:
Marcello Crosta

Relatore:
Chiar.mo Prof.
Andrea Cimatti
Correlatori:
Prof. Roberto Saglia
Dott. Maximilian Fabricius

Appello IV
Anno Accademico 2018-2019

Abstract

HETDEX is a blind spectroscopic survey that is using use 78 fiber based integral field units to search for Lyman Alpha Emitting galaxies (LAEs) in the high redshift universe. HETDEX will discover about half a million LAEs to measure cosmological parameters of the young universe. An important ingredient to this is the precise quantification of the velocity offsets of the Lyα emission form their corresponding host systems. The latter can be measured from other optical emission lines.
Here we present the results from VLT/KMOS near-infrared spectroscopic follow-ups of 8 Lyman-alpha emitters (LAEs) at $z = 2.1 - 2.5$ in the COSMOS field discovered by HETDEX. Observations are performed in the HK band. For these eight LEAs we detect rest-frame optical nebular lines Hα, [OIII]$\lambda\lambda$4960, 5008, for three of them we detect Hβ and for one [NII]λ6585. For non detected lines we measure a 1σ upper limit. We derive LAEs physical properties, including the Lyα velocity offset, star formation rate (SFR), gas-phase metallicity. Seven LAEs show a velocity shifts of Lyα relative to the systemic redshift ranging between +126 and +367 km s^{-1} with an average of +281 km s^{-1}. By matching KMOS^{3D} and HETDEX catalogs we measure velocity offsets for 2 more LAEs finding a mean velocity shift of +247 km s^{-1}. The velocity offsets we measure from these two independent samples are compatible to Song et al. (2014). The Lyα velocity offsets show a moderate correlation with the measured SFR. We show that Lyα radiative transfer effects influence the correlation function measurements at $s < 10$ h^{-1} Mpc.

Contents

Chapter 1

Introduction

1.1 Lyman Alpha Emitters

Lyman-alpha emitters (LAEs) are galaxies selected by their strong Lyα emission line. Lyα emission line has a vacuum rest-frame wavelength of 1215.67$\mathring{A}$ and it is intrinsically the brightest line emitted from active galaxies in the rest-frame UV and optical. Lyα is emitted from ionised hydrogen around star-forming regions and AGN. This line is a powerful feature to detect and study high redshift galaxies and the clustering of Lyα emitters allows us to probe cosmology at high redshifts.
Until recently bright LAEs were only discovered in relatively low numbers, because the preferred observing technique of using narrow band filters could only probe a limited redshift range. With the advent of large integral field unit instruments, blind spectroscopic searches allow for the search of these objects on a much larger redshift range. This was recently demonstrated by the Multi Unit Spectroscopic Explorer (MUSE) instrument finding 237 LAEs in a survey of the COSMOS field (Herenz et al., 2017) and the Mitchell Spectrograph at the McDonald 2.7m telescope finding a total of 104 LAEs also in the COSMOS field in the Pilot Survey (HPS) (Adams et al., 2011; Blanc et al., 2011) of the Hobby-Eberly Telescope Dark Energy Experiment (HETDEX) (Hill et al., 2008). Through its multiplexed integral field units (IFUs) the HETDEX survey will increase the LAE sample size by orders of magnitude, up to 0.8 million, and for the first time allow us to use their spatial distribution to derive cosmological parameters in the high redshift universe, and to study the physical properties of these objects in a statistically meaningful fashion.
LAEs appear to be predominately young, low-mass and low in dust extinction. Some works show that the LAE population contains a subset of systems containing a moderate amount of dust (Guaita et al., 2011). It is interesting that we observe strong Lyα from dusty systems because in a static homogeneous medium the resonant nature of Lyα should make practically impossible to escape if dust is present. One way to enable the escape of Lyα photons even with the presence of dust is the presence of outflows. This bulk motion of neutral gas can help the escape of Lyα photons by redshifting the Lyα photons out of resonance and reducing the number of resonant scatterings that they undergo before escape. Numerical modeling of Lyα radiative transfer in a simplified expanding shell scenario (Verhamme et al., 2006) predicts that Lyα photons escape redshifted respect to the systemic redshift, which can be measured from nebular lines (as Hα or [OIII]λ5008) originated from the HII regions but not resonantly scattered as Lyα. The predicted Lyα offset from systemic redshift has

been shown in different works (Hashimoto et al., 2013; Song et al., 2014). Figure 1.1 from Verhamme et al. (2006) shows the expected Lyα line profile in an expanding shell model with a central monochromatic source. The red peak produced by photons which undergo one backscatter is the highest expected peak but it isn't the only feature, parameters driving the Lyα profile in this model are the velocity of the expanding shell, the neutral hydrogen column density and the amount of dust. The details of this process are however poorly understood and model spectra only partially resemble observed data. Chonis et al. (2013) studied three sources selected from the HPS survey but observed with three times spectral resolution than in HPS, and they demonstrate that while the double peak structure of the Lyα is very similar across their three targets, several significant discrepancies between the standard expanding shell model and these data exist.

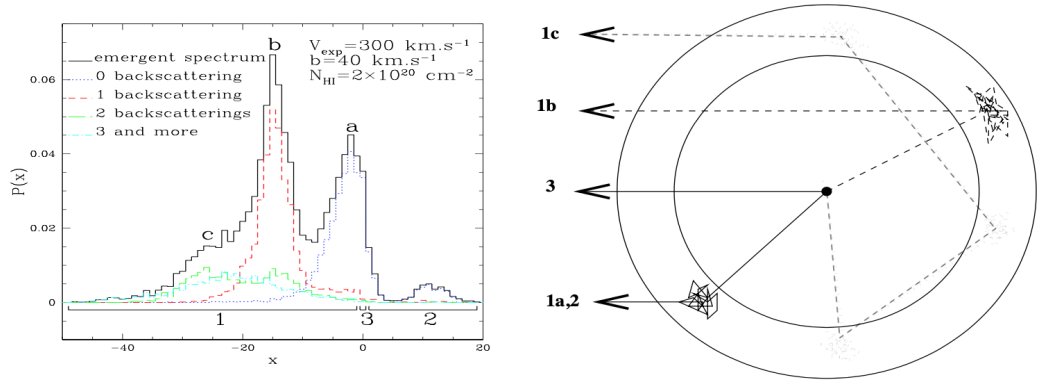

Figure 1.1: From Verhamme et al. (2006). The expected emergent Lyα line profile from an expanding shell with central monochromatic source. The x-axis is in doppler units $x = \frac{\nu - \nu_0}{\Delta\nu_D}$, where ν is the frequency of the escaping photon, ν_0 is the Lyα line frequency and $\Delta\nu_D$ is the Doppler frequency width due to the velocity dispersion. A negative x corresponds to a redshift from the systemic redshift. The different shapes can be described with the number of backscatterings Lyα photons undergo: bumps $1a$ and 2 are built-up with photons which undergo no backscattering, the highest peak is composed by photons which undergo one backscattering and the red tail is made of photons which undergo two or more backscattering. On the right there's a scheme of the expanding shell showing the origin of photons. In this picture the observer is on the left side at infinity.

Another scenario proposed in addition to kinematics to enhance the escape of Lyα photons is a multi-phase inter stellar medium (ISM) with an inhomogeneous dust distribution (Hansen & Oh, 2006). In this model dust is confined in clumps of neutral gas and Lyα photons suffer little dust attenuation by resonantly scattering off on the surface of gas clouds and this enhance their chance to escape. The continuum photons don't resonantly scatter on the clumps surface and suffer dust attenuation. This model was first observationally studied by Finkelstein et al. (2008), this and later studies (Blanc et al., 2011; Song et al., 2014) support the hypothesis of a quasi-clumpy ISM where dust doesn't attenuate Lyα more than UV continuum.
Metallicity appears to be an important factor in governing the escape of Lyα photons. This property is, however, still poorly understood for LAEs at redshift ~ 2 because near infrared spectroscopy is required to directly measure metallicity using rest-frame optical emission lines at this redshift. We have hints (Song et al., 2014) that LAEs have lower metallicity than continuum selected star-forming galaxies.

The Lyα emission line has been shown to be offset systematically from the systemic redshift, as it is expected from the expanding shell model, by several hundreds km s^{-1} (Hashimoto et al., 2013; Song et al., 2014). Recent works indicate that LAEs have a smaller Lyα velocity offset than continuum selected star-forming galaxies (Song et al., 2014). But results are tenuous because the LAE sample size is small. Lyα velocity offsets seem to correlate with the star formation rate (SFR) (Song et al., 2014) and anti-correlate with the Lyα equivalent width (Hashimoto et al., 2013).
The correction for the Lyα velocity offset is necessary to use LAEs is cosmology, as described in the next Section.
This thesis project is based on a previous HPS follow-up project described in Song et al. (2014). They obtained rest-frame optical spectroscopy of 17 purely Lyα selected LAEs in the HETDEX pilot survey ($2.1 < z < 2.5$). Observations for 10 of their targets were performed with the Spectrograph for Integral Field Observations in the Near Infrared (SINFONI) at the VLT and for the other seven targets with the Near Infrared Spectrograph (NIRSPEC) at the Keck telescope. They measure the Lyα velocity offset for 10 objects, with an average of 196 km s^{-1}. For these 10 LAEs they measure a metallicity upper limit using the N2 index from Pettini & Pagel (2004). Their results indicate that these LAEs are relatively metal poor, with at least one object falling significantly below the $z \sim 2.3$ mass metallicity relation for continuum selected star-forming galaxies from Erb et al. (2006). They find a positive correlation between the Lyα velocity offset and the SFR but no clear correlation for the Lyα velocity offset with stellar mass, dynamical mass, specific SFR, SFR surface density and Lyα equivalent width. Their results support the hypothesis of a quasi-clumpy ISM where Lyα radiation is attenuated by the dust as the UV continuum.

1.2 Galaxy clustering measurements with LAEs

Galaxy surveys can provide an accurate view of the large-scale galaxy clustering pattern and they can be used to put new constraints on the dark energy properties and the curvature of the Universe (Sanchez, 2020). The statistical analysis of the large-scale structure of the Universe is based on the galaxy density fluctuation field

$$\delta_g(\mathbf{x}) = \frac{\rho_g(\mathbf{x}) - \overline{\rho}_g}{\overline{\rho}_g}. \tag{1.1}$$

We can use measurements of the galaxy power spectrum to establish a link between observations and theoretical models.
The most used statistical tool in galaxy surveys is the two-point correlation function, $\xi(r)$, defined as

$$\xi(\mathbf{r}) = \langle \delta(\mathbf{x}) \delta(\mathbf{x} + \mathbf{r}) \rangle. \tag{1.2}$$

The correlation function depends only on the separation $r = |\mathbf{r}|$ because clustering is statistically isotropic. Expressing the density fluctuations in terms of their Fourier transform you find that the correlation function is the Fourier transform of the power spectrum:

$$\xi(r) = \frac{1}{(2\pi)^3} \int d^3k P(\mathbf{k}) e^{i\mathbf{k}\,\mathbf{r}}. \tag{1.3}$$

In a ΛCDM model the amplitude of the correlation function is expected to decrease with increasing scales. Measurements of the correlation function of galaxy samples are indicators of the galaxy clustering and the distribution of galaxies doesn't necessarily match

the underlying matter distribution. We can assume that galaxy density fluctuations are functions of the local matter density fluctuations, this effect is quantified by the bias parameter. In the linear regime, described by $\delta \ll 1$, this dependency is given by

$$\delta_g(\mathbf{x}) = b\delta(\mathbf{x}) \tag{1.4}$$

and the galaxy and matter correlation functions are related by

$$\xi_g(r) = b^2\xi(r). \tag{1.5}$$

It is possible to define the correlation function of a discrete set of points starting from the probability of finding a pair of galaxies at a given separation. For a general distribution the probability of finding a pair of points in two volume elements dV_1 and dV_2 separated by a given distance r_{12} is given by

$$dP = \langle \rho_1 \rho_2 \rangle dV_1 dV_2. \tag{1.6}$$

Expressing the densities as $\rho_i = \overline{\rho}(1 + \delta_i)$ this can be rewritten as

$$dP = \overline{\rho}^2(1 + \langle \delta_1 \delta_2 \rangle) dV_1 dV_2 = \overline{\rho}^2(1 + \xi(r_{12})) dV_1 dV_2. \tag{1.7}$$

This means that the correlation function gives the excess probability of finding pairs of galaxies separated by a distance r, with respect to a homogeneous distribution.
The estimation of the correlation function from a galaxy survey is based on Equation 1.7, but the characteristics of the survey depend on the selection function, $\phi(\mathbf{x})$, which gives the relation between the true and the observed density fields:

$$n_{obs}(\mathbf{x}) = \phi(\mathbf{x}) n_{true}(\mathbf{x}). \tag{1.8}$$

It is essential to compute the correct characterization of the selection function to obtain unbiased measurements from a galaxy survey. All correlation function estimators are based on a sample of random points corresponding to a homogeneous spatial distribution observed through the same selection function of the real data. The estimation of the correlation function depends on the probability of finding galaxy pairs separated by distances between r and $r + dr$. That is

$$DD(r) = \frac{N_{pairs}(r)}{N_{tot}}, \tag{1.9}$$

Where $N_{tot} = N_{gal}(N_{gal} - 1)/2$ is the total number of galaxies pairs. The probability of finding pairs of points in a homogeneous distribution, $RR(r)$, can be computed in an analogous way by means of the random catalog. $DR(r)$ is the probability of finding pairs of points one from the observed catalog and one from the random catalog. The most used correlation function estimator in current clustering analysis is

$$\hat{\xi}(r) = \frac{DD(r) - 2DR(r) + RR(r)}{RR(r)} \tag{1.10}$$

from Landy & Szalay (1993).

1.2.1 Redshift space distortions

The distances are inferred from the measured redshift in spectroscopic surveys. In a homogeneous Universe the redshift of a galaxy would be given purely by the cosmological

expansion. This would provide an accurate estimation of distances given a fiducial cosmology. In reality, the Universe has inhomogeneities and these induce peculiar velocities to the galaxies. This introduces an extra component to the measured redshifts and gives rise to a difference between the real and the apparent position of a galaxy. This leads to a change in the shape and amplitude of the measured two-point correlation function with respect to their real-space counterparts. This effect is known as redshift space distortions (RSD). However, as peculiar velocities are due to inhomogeneities in the density field, the pattern of RSD contains information on the matter distribution producing the distortion. That can be used to study the rate at which cosmic structures grow, offering a test to detect potential deviations from the predictions of general relativity.
The observed redshift of a galaxy is given by the combination of the cosmological redshift and the Doppler effect caused by the peculiar velocity:

$$(1 + z_{obs}) = (1 + z_{cos})(1 + z_{pec}). \tag{1.11}$$

Where z_{cos} is the cosmological redshift, it is due only to the expansion of the Universe and $z_{pec} = v_{\parallel}/c$ is the contribution due to the Doppler effect caused by the component of its peculiar motion along the line of sight direction. As it is shown in Figure 1.2, galaxies move away from underdense regions and towards overdense regions. There regions appear respectively elongated and contracted along the line of sight in the redshift space. This introduces a pattern of anisotropies in the clustering of galaxies. The full characterization of the apparent anisotropies in the clustering of galaxies caused by RSD requires to express the correlation function in terms of the components of the full separation vector $\mathbf{s}$ in the directions perpendicular and parallel to the line of sight $s_{\perp}$ and $s_{\parallel}$, that is $\xi(\mathbf{s}) = \xi(s_{\perp}, s_{\parallel})$. Otherwise the correlation function can be expressed in polar coordinates as $\xi(s, \mu)$, where s is total separation and μ is the cosine of the angle between the separation vector $\mathbf{s}$ and the line of sight direction. The same is applied to the power spectrum too. The power spectrum needs to be expressed as a function of the components of $\mathbf{k}$ in the perpendicular and parallel line of sight directions: $P(k_{\perp}, k_{\parallel})$ or as $P(k, \mu_k)$.

The density fluctuations in the redshift space, in the linear regime and assuming the distant observer approximation, can be writtern as

$$\delta^s(\mathbf{k}) = \delta(\mathbf{k})(1 + f(z)\mu_k^2). \tag{1.12}$$

Where $\mu_k = k_3/k$ represents the cosine of the angle between the wavevector $\mathbf{k}$ and the line of sight direction, and $f(z)$ is the logarithmic growth factor. Equation 1.12 shows that the density fluctuations in the redshift space correspond to that in the real space with a positive correction. The correction depends on μ_k, it is maximum when it is parallel to the line of sight direction ($\mu_k = 1$) and it is minimum when it is perpendicular to the line of sight ($\mu_k = 0$). The anisotropic power spectrum is given by

$$P^s(k, \mu_k) = \langle |\delta^s(k, \mu_k)|^2 \rangle = (1 + f(z)\mu_k^2)^2 P(k). \tag{1.13}$$

This relation implies that it is possible to extract the logarithmic growth factor $f(z)$ by studying the pattern of anisotropies caused by RSD. The growth rate, from general relativity, can be described by $f(z) = \Omega_m^{\gamma}$ with $\gamma = 0.55$.
You have to take into account that galaxies are biased tracers of the matter density distribution in the galaxy power spectrum. Assuming a linear bias relation between the galaxy and matter density fluctuations, $\delta_g = b\delta_m$, and that the velocity field of galaxies correspond to that of total matter distribution, $\mathbf{v}_g = \mathbf{v}_m$, you find

$$\delta_g^s(\mathbf{k}) = \delta_g(\mathbf{k}) + \delta_m(\mathbf{k}) f(z)\mu_k^2 = \delta_g(\mathbf{k})(1 + \beta(z)\mu_k^2), \tag{1.14}$$

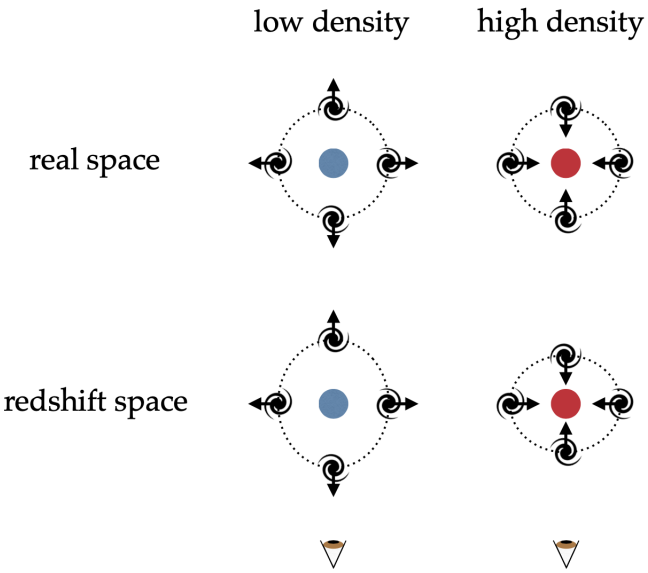

Figure 1.2: Schematic representation of the redshift space distortion effect on large scales. Galaxies move away from underdense regions and towards overdense regions. There regions appear respectively elongated and contracted along the line of sight in the redshift space.

where $\beta(z) = \frac{f(z)}{b}$ is the RSD parameter. The redshift space galaxy power spectrum is then given by

$$P_g^s(k,\mu_k) = b^2(1+\beta(z)\mu_k^2)^2 P_m(k) = \left(b\sigma_8(z) + f\sigma_8(z)\mu_k^2\right)^2 \left(\frac{P_m(k)}{\sigma_8^2(z)}\right), \tag{1.15}$$

where σ_8 measures the amplitude of the power spectrum on the scale of 8 h^{-1} Mpc. This expression shows that the amplitude and the shape of the redshift-space power spectrum is parametrized by the combination of $b\sigma_8(z)$ and $f\sigma_8(z)$. It is possible to constrain f and b from the pattern of anisotropies in the galaxies power spectrum using Equation 1.15.
It is useful to expand the anisotropic power spectrum and the correlation function in terms of Legendre polynomials $L_\ell(\mu_k)$. The power spectrum can be decomposed as

$$P_g^s(k,\mu_k) = \sum_{\ell\ even} P_\ell(k) L_\ell(\mu_k), \tag{1.16}$$

where the coefficients $P_\ell(k)$ correspond to the Legendre multipoles of the power spectrum and are given by

$$P_\ell(k) = \frac{(2\ell+1)}{2} \int_{-1}^{1} P(k,\mu_k) L_\ell(\mu_k) \mathrm{d}\mu. \tag{1.17}$$

All odd multipoles are zero because $P_g^s(k,\mu_k)$ is an even function. As in Equation 1.13 the maximum power of μ is 4, all multipoles with $\ell > 4$ will cancel. The decomposition of the power spectrum is

$$\frac{P_g^s(k,\mu_k)}{P_g(k)} = \left(1 + \frac{2}{3}\beta + \frac{1}{5}\beta^2\right) L_0(\mu) + \left(\frac{4}{3}\beta + \frac{4}{7}\beta^2\right) L_2(\mu) + \frac{8}{35}\beta^2 L_4(\mu). \tag{1.18}$$

The anisotropic correlation fuction is the Fourier transform of the power spectrum and it is possible to find a relation between the configuration space multipoles and their Fourier-space counterparts. Using these relations it is possible to find expressions for the Legendre

multipoles in configuration space. These are:

$$\xi_0(s) = \left(1 + \frac{2}{3}\beta + \frac{1}{5}\beta^2\right)\xi(s), \tag{1.19}$$

$$\xi_2(s) = \left(\frac{4}{3}\beta + \frac{4}{7}\beta^2\right)\left(\xi(s) - \overline{\xi}(s)\right), \tag{1.20}$$

$$\xi_4(s) = \frac{8}{35}\beta^2\left(\xi(s) + \overline{\xi}(s) - \frac{7}{2}\overline{\overline{\xi}}(s)\right), \tag{1.21}$$

where

$$\overline{\xi}(s) = \frac{3}{s^3}\int_0^s \xi(s')s^2 \mathrm{d}s, \tag{1.22}$$

$$\overline{\overline{\xi}}(s) = \frac{5}{s^5}\int_0^s \xi(s')s^4 \mathrm{d}s. \tag{1.23}$$

For LAEs we have to modify Equation 1.11 to consider the Lyα velocity offset as

$$(1 + z_{obs}) = (1 + z_{cos})(1 + z_{pec})(1 + z_{\mathrm{Ly}\alpha}), \tag{1.24}$$

where $z_{\mathrm{Ly}\alpha} = \Delta v_{\mathrm{Ly}\alpha}/c$ is the correction due to the Lyα velocity offset from the systemic redshift. In Chapter 7 we will use this correction to study the effect of the Lyα velocity offsets on the RSD.

In Chapter 2 we present the HETDEX survey and the Lyα data used in this study. In Chapter 3 we describe our near-infrared spectroscopic observations and data reduction for our sample of LAEs at $z = 2.1 - 2.5$. KMOS^{3D} data used in this work are presented in Chapter 4. Combining our NIR data, Lyα data and ancillary datasets, we present our measurements of LAEs physical properties in Chapter 5. In Chapter 6 we explore the mass-metallicity relation, mass-sSFR relation and we study the role of kinematics and geometry on the escape of Lyα photons. The effect of Lyα velocity offsets on the RSD is discussed in Chapter 7. Lastly, we summarize our results in Chapter 8.

Throughout this work, where is not explicetely told, we assume a standard ΛCDM cosmology with $H_0 = 70$ km s^{-1} Mpc^{-1}, $\Omega_M = 0.3$ and $\Omega_\Lambda = 0.7$.

Chapter 2

HETDEX

This thesis work is a follow up project of the Hobby-Eberly Telescope Dark Energy Experiment (HETDEX[1] (Hill et al., 2008; Gebhardt et al., in prep)). HETDEX is a blind survey of a 420 deg^2 area in the north Galactic cap. The survey will detect 0.8 million Lyman-alpha emitting (LAE) galaxies with $1.9 < z < 3.5$ and more than a million [OII] emitting galaxies with $z < 0.5$. HETDEX has the goal of providing constraints on the expansion history of the universe (the Hubble parameter H(z) and angular diameter distance $D_A(z)$) over redshifts z=1.9 to 3.5. HETDEX will use a combination of baryonic acoustic oscillations (BAOs) and power spectrum shape information to provide a direct detection of dark energy density over these redshifts. HETDEX data are obtained using the Visible Integral-field Replicable Unit Spectrograph (VIRUS[2]), which is fed by fibers from the prime focus of the upgraded 10 m Hobby-Eberly Telescope (HET[3]). The HET (Ramsey et al., 1994) is a telescope with 11 meter segmented primary mirror, located in West Texas at the McDonald Observatory. Recently it had a wide field upgrade (WFU Hill et al. (2018a)) that substantially increased the field of view to 21′. VIRUS (Hill et al., 2018a) is a massively replicated integral field spectrograph (Hill, 2014), designed for blind spectroscopic surveys. It consists in 78 integral field units (IFUs), each with 448 fibers of 1.5″ diameter. VIRUS has a fixed spectral bandpass of 350-550 nm and resolving power R $\sim$ 800 at 450 nm. Each IFUs feeds two spectrograph units and covers 50×50 arcsec^2 area for each unit. The fibers are illuminated directly at the prime focus of HET and are arrayed with a 1/3 fill-factor such that an observation requires three exposures with dithers in sky position to fill in the areas of the IFUs. A detailed technical description of

[1]HETDEX is led by the University of Texas at Austin McDonald Observatory and Department of Astronomy with participation from the Ludwig-Maximilians-Universität München, Max-Planck-Institut für Extraterrestriche-Physik (MPE), Leibniz-Institut für Astrophysik Potsdam (AIP), Texas A&M University, Pennsylvania State University, Institut für Astrophysik Göttingen, The University of Oxford, Max-Planck-Institut für Astrophysik (MPA), The University of Tokyo, and Missouri University of Science and Technology. In addition to Institutional support, HETDEX is funded by the National Science Foundation (grant AST-0926815), the State of Texas, the US Air Force (AFRL FA9451-04-2-0355), and generous support from private individuals and foundations. http://www.hetdex.org/

[2]VIRUS is a joint project of the University of Texas at Austin, Leibniz-Institut für Astrophysik Potsdam (AIP), Texas A&M University, Max-Planck-Institut für Extraterrestriche-Physik (MPE), Ludwig-Maximilians-Universität München, The University of Oxford, Pennsylvania State University, Institut für Astrophysik Göttingen, and Max-Planck-Institut für Astrophysik (MPA)

[3]The observations were obtained with the Hobby-Eberly Telescope (HET), which is a joint project of the University of Texas at Austin, the Pennsylvania State University, Ludwig-Maximilians- Universität München, and Georg-August- Universität Göttingen.

the HET WFU and VIRUS is presented in Hill et al. (2020).

2.1 HETDEX Data

Spectra present in the HETDEX first data release (hdr1) are calibrated using air wavelengths and aren't corrected for heliocentric velocity. We correct for the baryocentric velocity using the code described in Wright & Eastman (2014) and we convert HETDEX spectra from air to vacuum wavelengths because KMOS spectra are calibrated using vacuum wavelengths. For this conversion we use relations from Morton (2000):

$$\lambda_{vac} = n \times \lambda air \tag{2.1}$$

$$n = 1 + 0.0000834 + \frac{0.0240893}{130.1065925 - s^2} + \frac{0.0001600}{38.9256879 - s^2} \tag{2.2}$$

where $s = 10^4/\lambda_{air}$. This correction is wavelength dependent and n ranges from 1.000277 at 550 nm to 1.000286 at 350 nm. At 450 nm Equation 2.1 corresponds to $\lambda_{vac} = 1.000281 \times \lambda_{air}$.
COSMOS is a deep, multi-wavelength survey aimed at measuring the evolution of galaxies. The COSMOS survey is centered at (J2000): R.A. 10:00:28.60 Dec. +02:12:21.0 and the COSMOS field cover a 2 square degree region around this center. The field has been observed at all accessible wavelengths from the X-ray to the radio with most of the major space-based and ground based telescopes. We select our targets in this region in order to use also data from this catalog in our analysis.
In the COSMOS field HETDEX observes sometimes the same region more than once. For this reason we have multiple exposures for some LAEs. If a LAE has multiple observations we first correct the wavelength calibration for every exposure and we then combine the different spectra to improve the SNR. In Figure 2.1 are shown spectra of Object 1 for the five different exposures present in the HETDEX catalog. Figure 2.2 shows the Lyα detection for the 8 sources that have a near-infrared counterpart that we observed with KMOS. Table 2.1 summarizes the Lyα properties from HETDEX for the 8 LEAs with a near-infrared counterpart. In particolar are reported here the position, Lyα flux and Lyα redshift.

Table 2.1

Object	*R.A.* ($J2000$)	*Dec.* ($J2000$)	$F_{\mathrm{Ly}\alpha}$ (10^{-17} erg s^{-1} cm^{-2})	$z_{\mathrm{Ly}\alpha}$
1	10:00:57.48	02:18:00.7	36.16 ± 2.20	2.1646 ± 0.0002
2	10:00:39.61	02:15:38.1	22.34 ± 1.22	2.4548 ± 0.0002
3	10:00:44.80	02:13:55.0	26.12 ± 2.09	2.1773 ± 0.0003
4	10:00:47.16	02:13:04.9	26.06 ± 1.59	2.3416 ± 0.0003
5	10:00:56.86	02:13:16.6	21.02 ± 1.10	2.4345 ± 0.0002
6	10:00:57.48	02:15:24.6	18.16 ± 1.32	2.8818 ± 0.0002
7	10:01:00.46	02:16:13.5	28.12 ± 4.84	2.0985 ± 0.0005
8	10:01:00.87	02:17:28.2	13.08 ± 0.80	2.4708 ± 0.0002

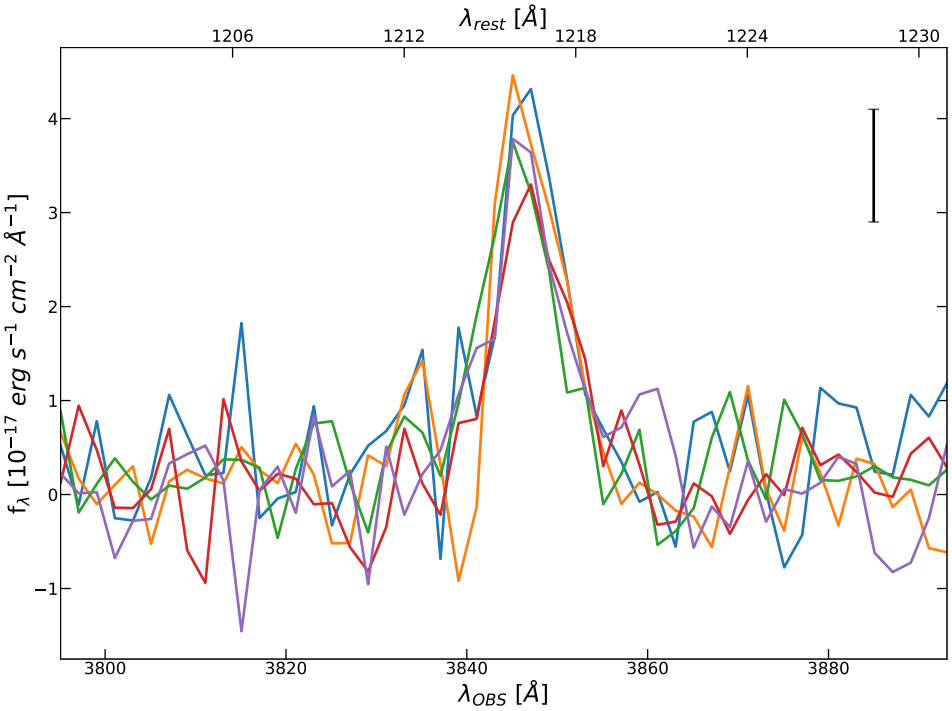

Figure 2.1: The five Lyα detections present in the HETDEX catalog for LAE 923. These spectra are calibrated in air wavelength and aren't corrected for heliocentric velocity. In the top right corner is shown the average error for these five spectra.

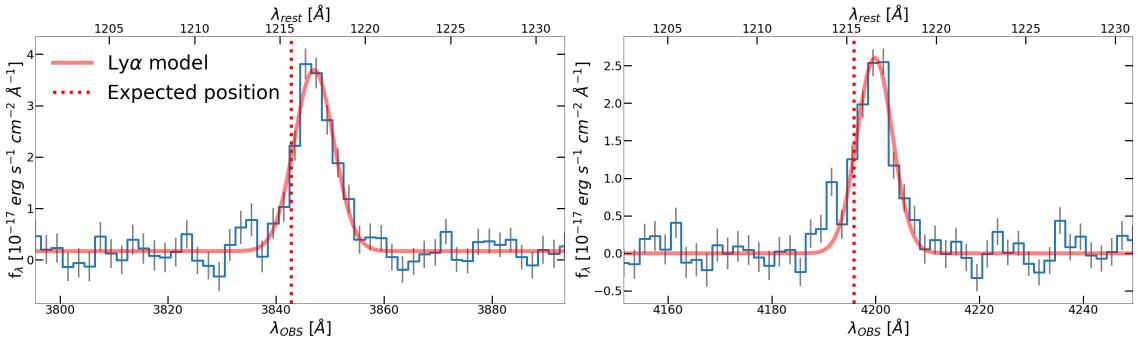

(a) Object 1 **(b)** Object 2

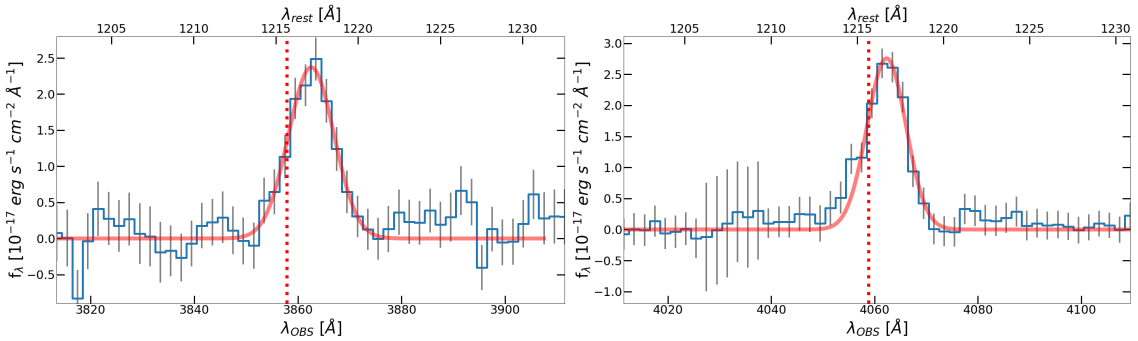

(c) Object 3 **(d)** Object 4

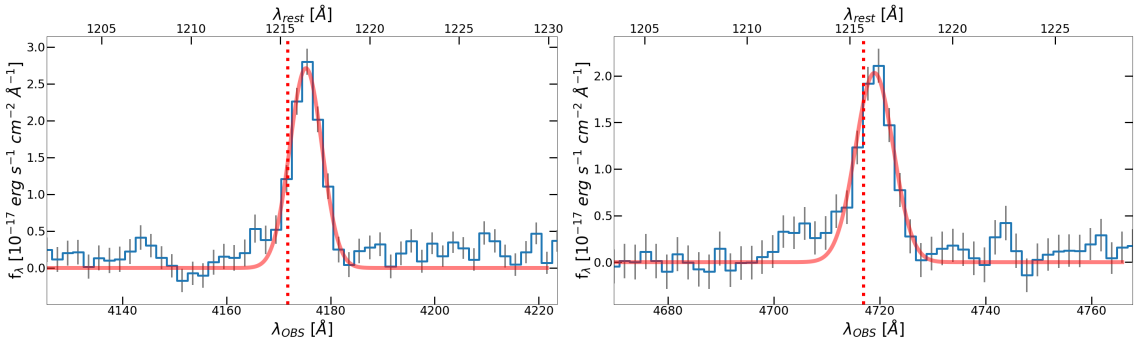

(e) Object 5 **(f)** Object 6

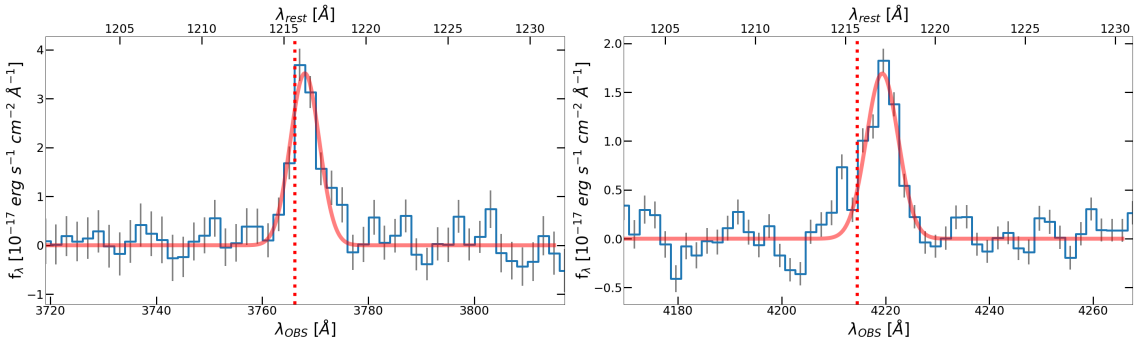

(g) Object 7 **(h)** Object 8

Figure 2.2: HETDEX spectra around Lyα for the 8 LAEs with a near-infrared counterpart observed with KMOS. The best-fit single Gaussian is overplotted in red. The red dotted vertical line is the expected position extracted using the systemic redshift. These spectra are the weighted average of the multiple exposures present in the HETDEX catalog and every exposure was corrected for the heliocentric velocity and wavelength converted from air to vacuum wavelength.

Chapter 3

KMOS

3.1 Sample selection

We selected LAEs from the first HETDEX data release (hdr1) that are present in the COSMOS field. We focused on LAEs that have redshift such that the [OIII] line falls in the H band ($1.9 < z < 2.7$) or the Hα line falls in the K band ($2 < z < 2.7$). The sample we consider contains $\sim$ 150 different objects. In correspondence of every emission line (Hβ, [OIII], Hα and [NII]) in a 10$\mathring{A}$ wide window we put a threshold in the average atmospheric transmission (T_{thre}) and the sky background (E_{thre}). We base this on a typical night sky from ESO's skycalculator online tool. We put a constrain on the minimum HETDEX Lyα flux. We form three lists asking different thresholds on the these three parameters. The A-list contains 53 high fidelity targets ($E_{thre} < 10^5$, $T_{thre} > 0.7$, $f_{\mathrm{Ly}\alpha} > 10 \times 10^{-17}\ erg\ cm^{-2}\ s^{-1}$). The B-list contains 38 targets that aren't present in A-list. B-list's targets fainter or in correspondence of more intense sky emission line than those in A-list ($E_{thre} < 5 \times 10^5$, $T_{thre} > 0.5$, $f_{\mathrm{Ly}\alpha} > 5 \times 10^{-17}\ erg\ cm^{-2}\ s^{-1}$). The C-list contains all the other targets. For our two KMOS pointings we select the two 7.2 arcmin diameter regions that contain the largest number of objects from the A-list. We adjust the pointing center to include as many B-list objects as possible. Finally we add all the remaining C-list targets. The fields of view of the two KMOS pointings are shown in Figure 3.1. Figure 3.2 shows in the I-band and in the Ks-band the objects we observed.

3.2 KMOS observations

We performed our observations with the K-band Multi Object Spectrograph (KMOS), this is a multi object image slicer spectrograph on the Very Large Telescope array (VLT). VLT is located in Chile at the Paranal Observatory, it is composed by four Unit Telescopes (UT), each with a 8.2 m diameter primary mirror. KMOS works at a Nasmyth focal plan of UT1. KMOS is designed to perform Integral Field Spectroscopy in the near-infrared bands for 24 targets simultaneously. The observed sub-fields are fed to 24 image slicer integral-field units (IFUs) that partition each sub-field into 14 identical slices, with 14 spatial pixels along each slice. KMOS has three cryogenic grating spectrometers and they work on eight IFUs each. Every exposure generates 14×14 spectra for every IFU.
Targets can be selected in a 7.2$'$ diameter circle, it is the diameter of the unvignetted field at the VLT Nasmyth focus. Each IFU has a square $2.8'' \times 2.8''$ field of view. In addition to observing multiple individual sources, KMOS has the capability for integral field mapping

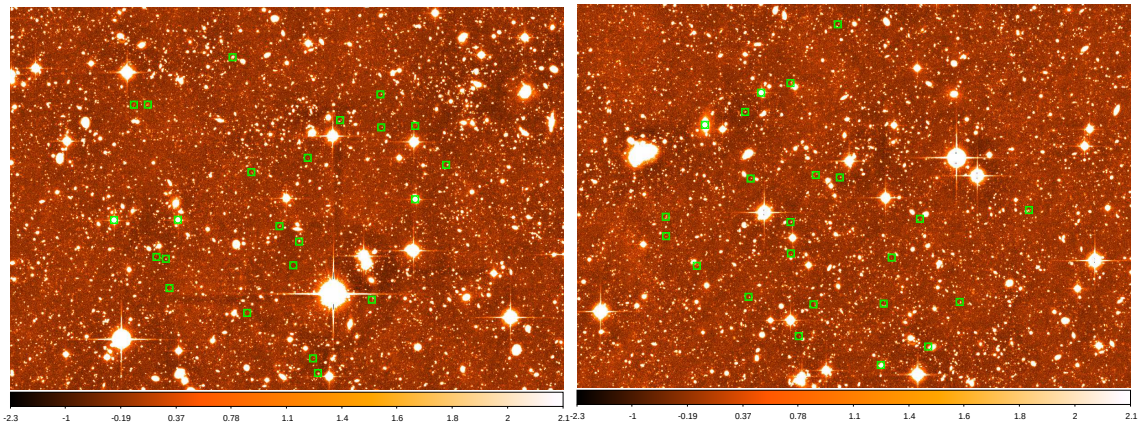

(a) First pointing **(b)** Second pointing

Figure 3.1: Targets position for the two KMOS pointings. The stars selected are used to compute the PSF model and to perform the flux calibration.

of contiguous areas in an 8-point or 16-point dither pattern. KMOS can observe in the IZ, YJ, H, K bands with an average resolving power of ~ 3800. It is possible to observe the H+K bands simultaneously with a resolution of 2000. Our KMOS observations are all performed in this HK band.
Our observations had a mean point-spread function (PSF) full-width at half-maximum (FWHM) of ~ 0.6". This corresponds to a physical scale of ~ 6 kpc at $z \sim 2.3$, which is much larger than the typical size of < 2 kpc for LEAs at similar redshift in rest-frame UV (Bond et al., 2012). We performed two pointings consisting of $39 \times 300s$ individual exposures, with dithering of an ABAABA pattern. Every object was observed in only one pointing. For telluric absorption correction, as well as flux calibration, in every field we observed three telluric standards stars.

3.3 Data Reduction

The data were reduced with the SPARK (Software Package for Astronomical Reduction with KMOS) software version 1.3.5 (Davies et al., 2013) and a set of custom IDL scripts (Wisnioski et al., 2019). The workflow for the data reduction is the same of Wisnioski et al. (2019). We present here the crucial parts of the pipeline and the modifications that we performed to the inhouse IDL scripts to perform a optimal data reduction for the HK band. In Wisnioski et al. (2019) they didn't observe in the HK band but only in the H and K bands separately, and this required minor changes on the IDL routine.

3.3.1 Sky subtraction and heliocentric correction

A number of techniques have been developed to address the problem of sky subtraction for ground-based spectroscopic measurements of faint objects. In most cases the methods leave behind narrow residual features which can hinder the detection and measurement of astronomical sources. These residuals come from the oversubtraction and undersubtraction of a modeled or interpolated sky emission spectrum. The residuals arise due to small variations in the characteristics of the instrument at different spatial positions and thus associated imperfections in the calibration process. Sky residuals are particularly

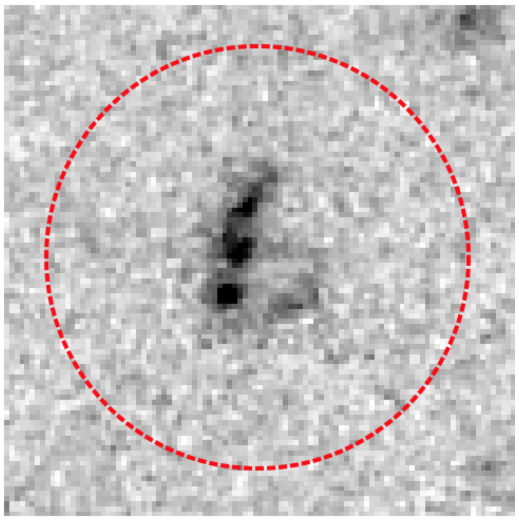

(a) Obj. 1 HST F814W - $3'' \times 3''$

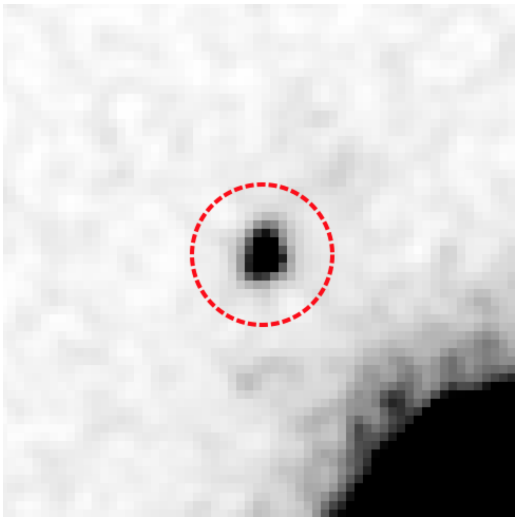

(b) Obj. 1 UVISTA Ks - $9'' \times 9''$

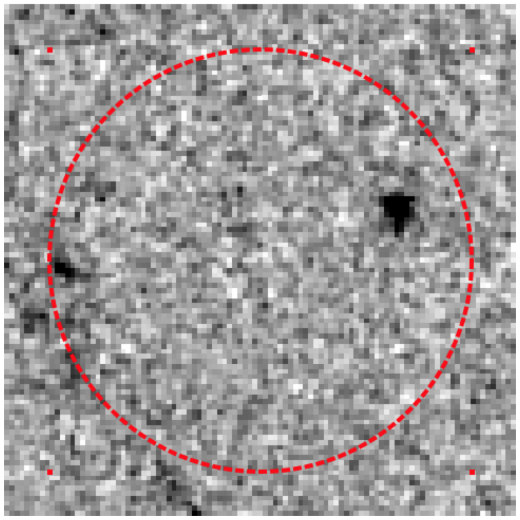

(c) Obj. 2 HST F814W - $3'' \times 3''$

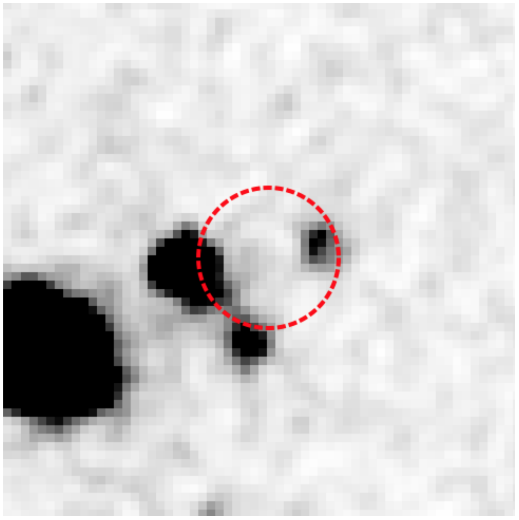

(d) Obj. 2 UVISTA Ks - $9'' \times 9''$

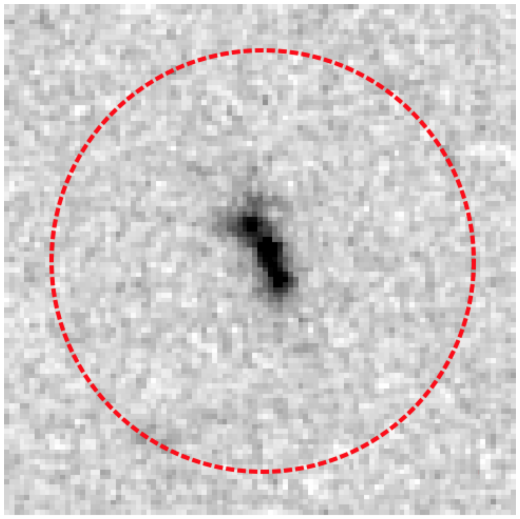

(e) Obj. 3 HST F814W - $3'' \times 3''$

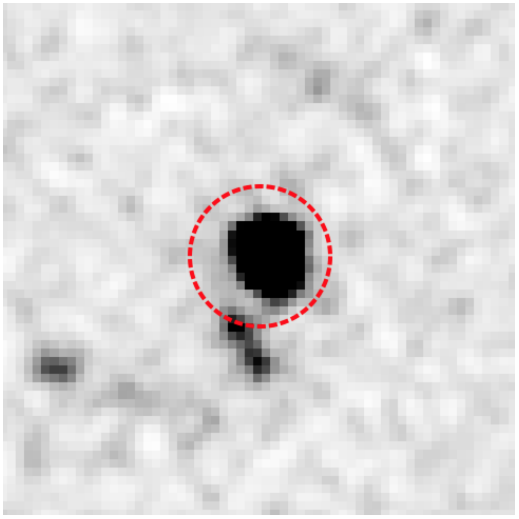

(f) Obj. 3 UVISTA Ks - $9'' \times 9''$

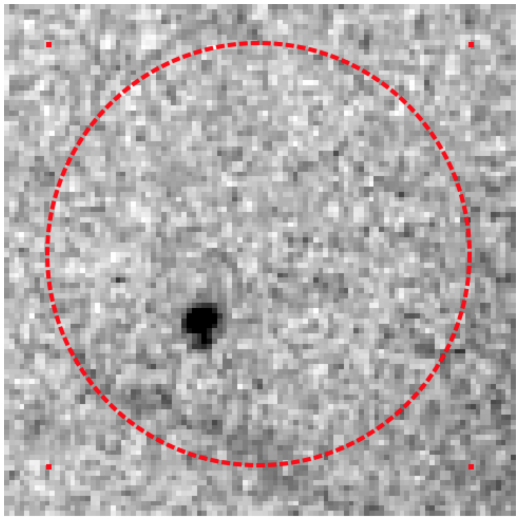

(a) Obj. 4 HST F814W - $3'' \times 3''$

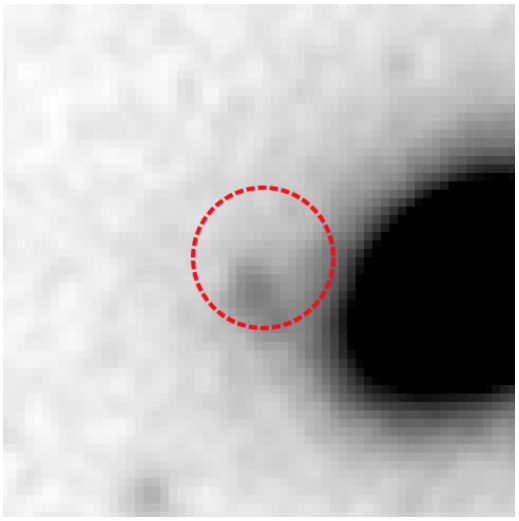

(b) Obj. 4 UVISTA Ks - $9'' \times 9''$

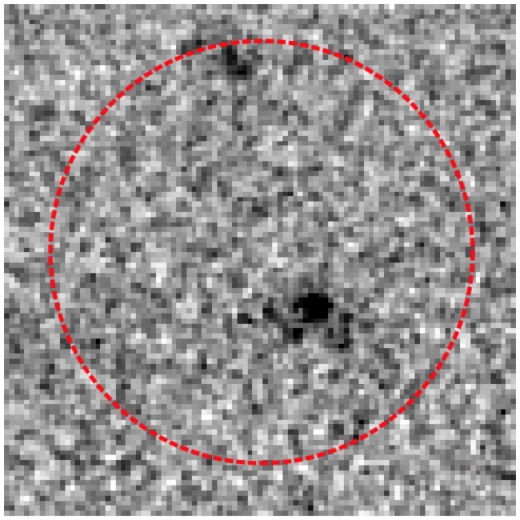

(c) Obj. 5 HST F814W - $3'' \times 3''$

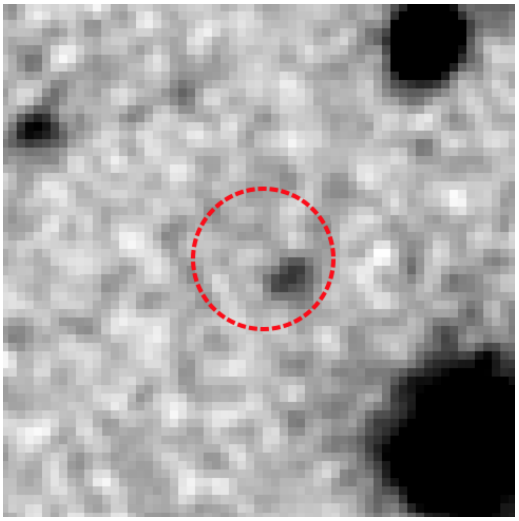

(d) Obj. 5 UVISTA Ks - $9'' \times 9''$

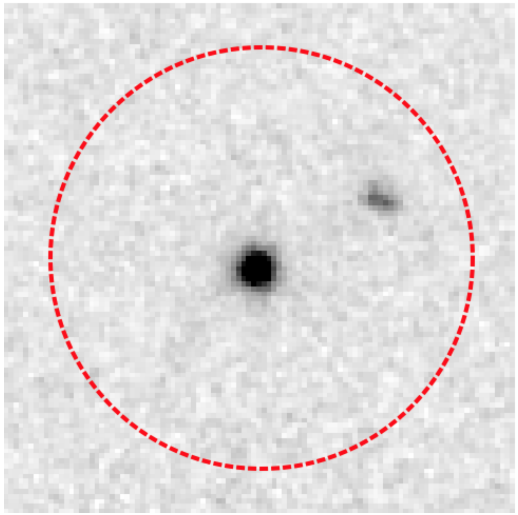

(e) Obj. 6 HST F814W - $3'' \times 3''$

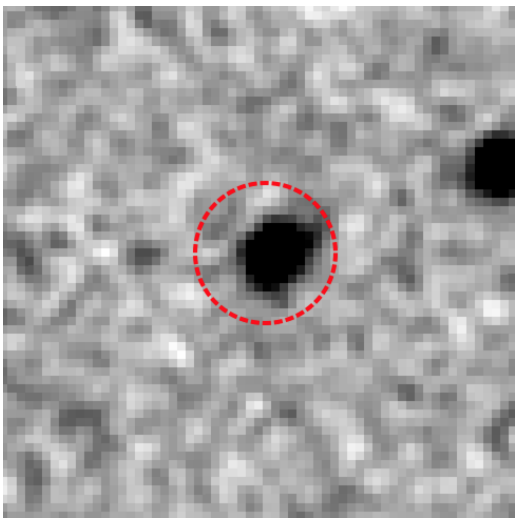

(f) Obj. 6 UVISTA Ks - $9'' \times 9''$

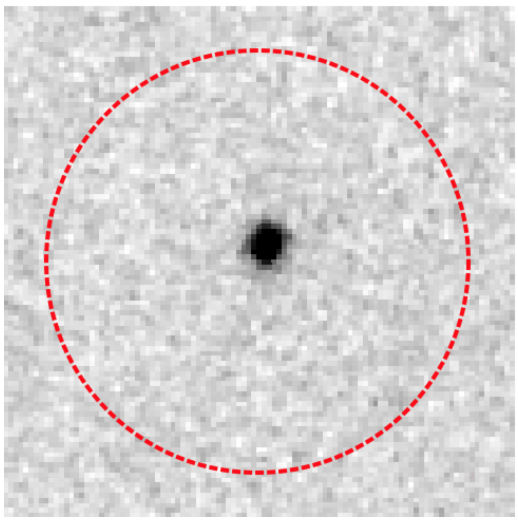

(a) Obj. 7 HST F814W - $3'' \times 3''$

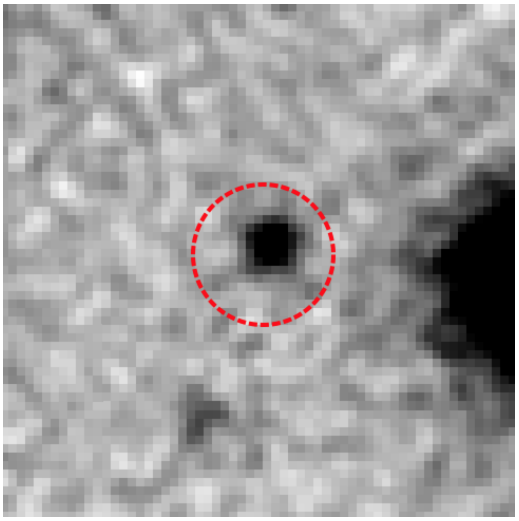

(b) Obj. 7 UVISTA Ks - $9'' \times 9''$

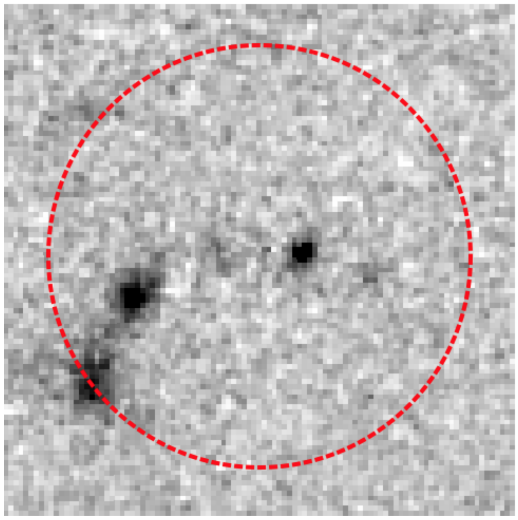

(c) Obj. 8 HST F814W - $3'' \times 3''$

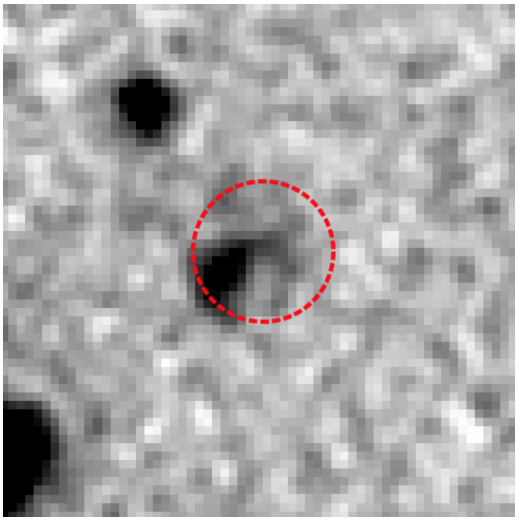

(d) Obj. 8 UVISTA Ks - $9'' \times 9''$

Figure 3.2: Cutout stamp images of our eight LEAs observed with KMOS. On the left $3'' \times 3''$ images from $HST/F814W(I)$. On the right $9'' \times 9''$ images from VISTA Ks. Red dotted circles have a $2''.5$ diameter and their center is the same of KMOS observations.

problematic where the background is rapidly changing with wavelength, i.e. around sky emission lines. KMOS is subject to similar problems.
We use the Zurich Atmosphere Purge (ZAP) (Soto et al., 2016) to perform the sky subtraction, it is designed to subtract residual sky features while minimizing the effect on astronomical signals. Through the use of principal component analysis (PCA) combined with filtering, ZAP constructs a sky residual spectrum for each individual spaxel which can then be subtracted from the original data cube. The central concept of PCA is to use the data itself to find a set of principal components that describe the variations over the residual sky spectrum and subtract them from the spectrum. We have considered all the KMOS HK-band sky exposures taken in a three month range from our observations. We have applied the detector and the illumination correction to these exposures and we have performed the PCA on these data. We then use the result of this PCA to perform the

ZAP sky subtraction for all our exposures. In Figure 3.3 is present a comparison for the sky subtraction using SPARK and ZAP.

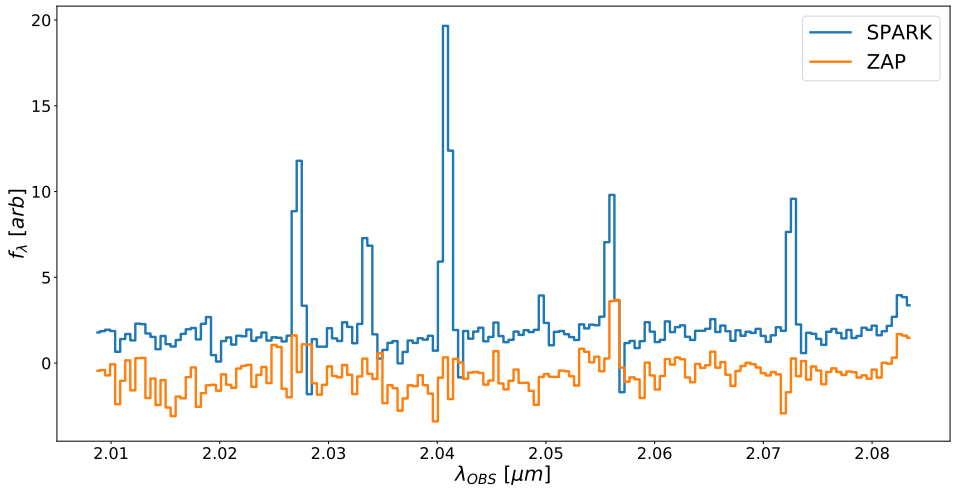

Figure 3.3: Comparison of the sky subtraction using ZAP and SPARK. In this wavelength regions no emission lines of LAEs are present. Blue emission lines are sky emission lines that SPARK can't optimally subtract. The shift between the two spectra is only for a better visualization.

A heliocentric correction is applied to all data frames before they are combined. Uncorrected data can lead to inaccurate redshifts and to inflated integrated velocity dispersions, particulary for narrow emission lines that are near the instrument resolution limits.

3.3.2 Illumination correction

The KMOS reduction pipeline performs a rotator angle dependent illumination correction done per object-sky pair using the internal flat with the closest rotator angle. The closest angle, of the six available (0°, 60°, 120°, 180°, 240°, 300°), provides the best illumination correction. This is crucial for the first observing block where objects and their adjacent sky are taken at a different rotator angle.

3.3.3 First pointing data reduction

The flat fielding correction depends on the rotator angle of the observation. Figure 3.4 shows flat fields taken for IFU 6 to perform the illumination correction, for every IFU they observe a flat field at six different angles (0°, 60°, 120°, 180°, 240°, 300°). Every exposure is corrected using the closest flat field observed.

A non uniform background illumination is present in every science data cube of the first pointing after the illumination correction and the sky subtraction. The reason of this effect is probably that every object frame and its adjacent sky frame are taken at different rotator angles, the illumination correction depends on this angle. In the second pointing, where object and sky frames are observed at similar rotator angles, this effect is not present. In Figure 3.5 the illumination gradient present in the first pointing is shown

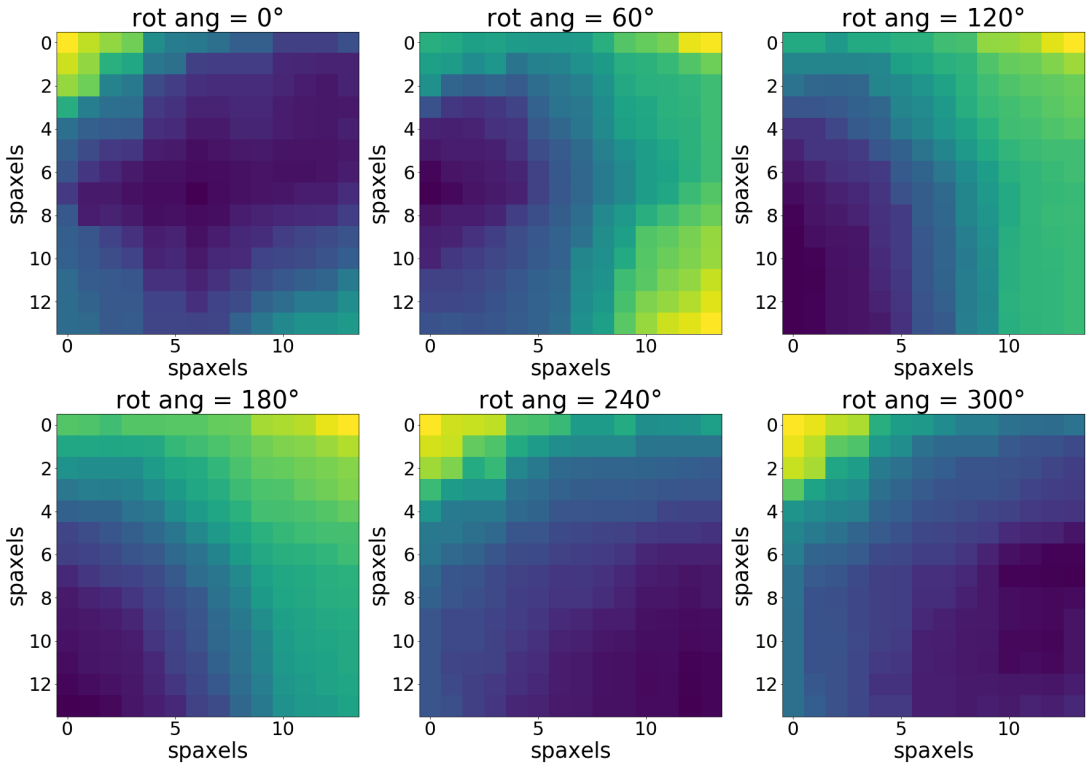

Figure 3.4: Flat fields taken for the IFU 6. Every IFU has a different instrumental response to a uniform illumination. Since this effect depends on the rotator angle of the exposure too flats fields are observed, starting from the top left corner, at 0°, 60°, 120°, 180°, 240°, 300° degrees and the illumination correction of every exposure is performed with the closest of these flat field.

together with a comparison with the homogeneous background of the second pointing. From the same image you can see that this effect is wavelength and IFU dependent.

We have tried to remove this effect by working on the pipeline. Interpolating the six different flat fields observed for every IFU we produce a matrix for the illumination correction for every rotator angle with an exposure. Normally the sky subtraction is performed before the illumination correction because the science frame is taken at a similar rotator angle to its adjacent sky frame. We have tried to perform the illumination correction before the sky subtraction, because in this case the corrections for the science and its sky frames are different, using the matrix corrections that we have generated. This procedure is unable to correct for this effect, a comparison between the results obtained using the usual KMOS pipeline and the pipeline with my changes are given in Figure 3.6 and Figure 3.7.

We also attempt to correct for this error by working directly on the data cubes produced after the sky subtraction. For every slice of data cubes we fitted the gradient with a plane and we divided the slice for its normalized plane. Also in this way data aren't completely flat, probably because a plane is a poor representation of the spatially varying illumination. We decided to focus our work only from objects from the second pointing.

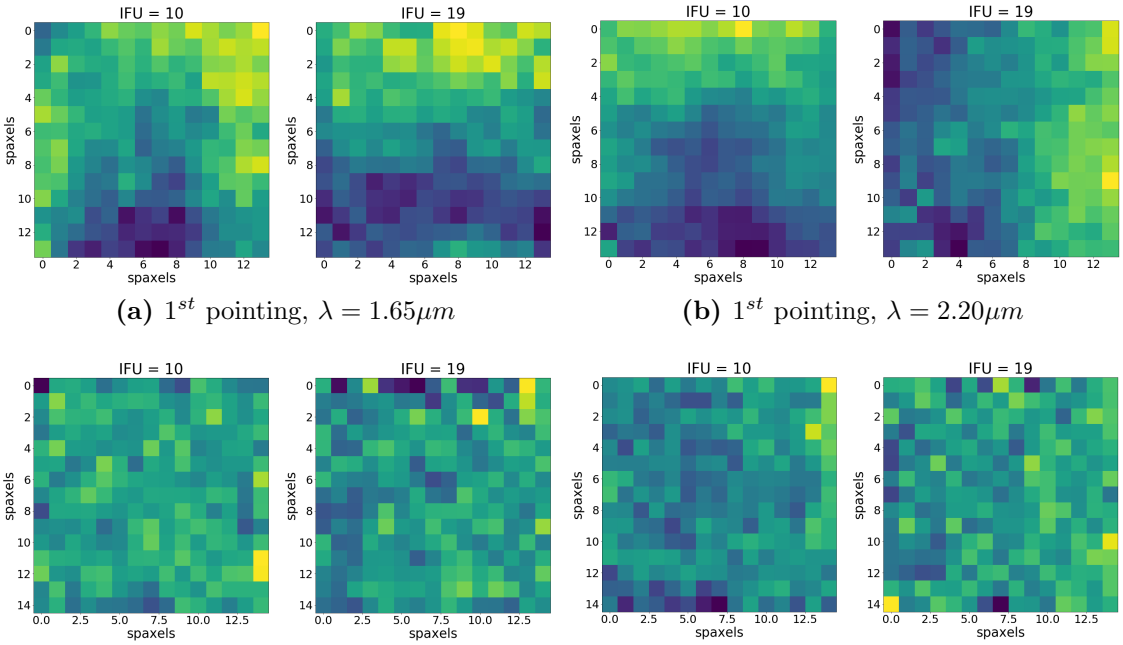

(a) 1^{st} pointing, $\lambda = 1.65\mu m$ **(b)** 1^{st} pointing, $\lambda = 2.20\mu m$

(c) 2^{nd} pointing, $\lambda = 1.65\mu m$ **(d)** 2^{nd} pointing, $\lambda = 2.20\mu m$

Figure 3.5: Background illumination comparison from slices of different data cubes for the two pointingss at different wavelength and in different IFUs. In every couple of images the left one is for IFU 10 and the second one for IFU 19. In (a) and (b) exposures are from the first field, in (c) and (d) exposures are from the second field.

3.3.4 Flux calibration

To perform the flux calibration a B8V star is observed at the end of every pointing. The observed 'standard' stars were selected from the Hipparcos catalog (Perryman et al., 1997) with known IR magnitudes (Cutri et al., 2003). The star observations are used to apply both a telluric transmission correction and flux calibration to all individual science frames. The standard KMOS observing procedure was followed such that a single standard star is observed in three IFUs, one per detector. Observed stars were chosen to be at similar airmass as the science data. Photometric zero points are calculated in the AB system using custom IDL routines. The observations of standard stars are collapsed to a 1D spectrum. The mean counts within the H-part ($1.484\mu m$ - $1.846\mu m$) and the K-part ($1.934\mu m$ - $2.442\mu m$) are used to derive the zero points for the H-band and the K-band part of the spectrum. A model Moffat function is fit to the stars to correct for the small fraction of flux lost outside of the IFU, tipically 1-3%. A telluric transmission spectrum is created by dividing the standard star spectrum by a blackbody function of the effective temperature of the standard star and removing the intrinsic stellar absorption features. Each spaxel is then divided by the telluric spectrum observed in the same detector. An airmass correction is applied to account for the difference in elevation between observations of the standard star and each science frame. The zero point is then applied to derive the absolute flux scale for each science frame.

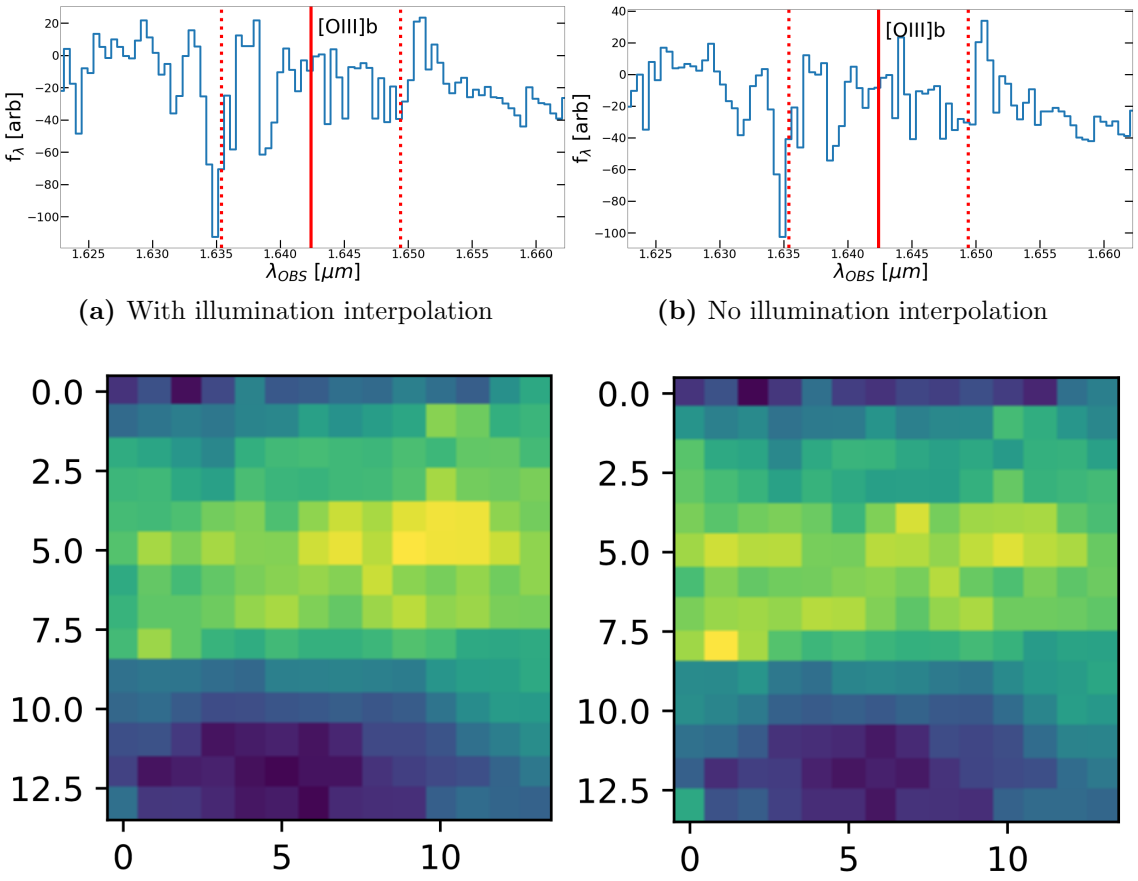

(a) With illumination interpolation

(b) No illumination interpolation

Figure 3.6: Comparison of the spectra, in correspondence of the expected [OIII]λ5008 emission line, obtained performing the illumination correction with the interpolation of the six flat fields (left) and without the interpolation (right). 2D images are obtained by summing spaxels over the wavelength range between red dotted lines shown in the 1D spectra. The red vertical line represents the expected [OIII]λ5008 emission line position.

3.4 1D Spectra

After the combination of the different exposures we have 20 science datacubes. We don't detect the expected LAE in every IFU, this is likely to the error in the HETDEX astrometry and the targets we add to our sample from the B and C lists described in Section 3.1. From the [OIII] and Hα images we individuate 8 LAEs (Figure 3.8) for which it is possible to extract the 1D spectrum. To extract the 1D spectrum from each cube where a LAE is detected, we used a 2D Gaussian model:

$$g = a \times e^{-\frac{1}{2}\left[\frac{(x-x_0)^2}{\sigma_x^2}+\frac{(y-y_0)^2}{\sigma_y^2}\right]} \tag{3.1}$$

where a is the Gaussian amplitude and is a free parameter of the model, σ_x and σ_y are given by the Gaussian PSF model of the three observed star and are respectively $0.31''$ and $0.29''$. The Gaussian center was determined by finding the centroid position in a 4-pixel boxcar [OIII] or Hα image. The 1D spectra optimal extraction is performed by fitting the 2D Gaussian model to every slice of the data cubes, with the amplitude as the only free parameter, and summing all the components of the 2D Gaussian.

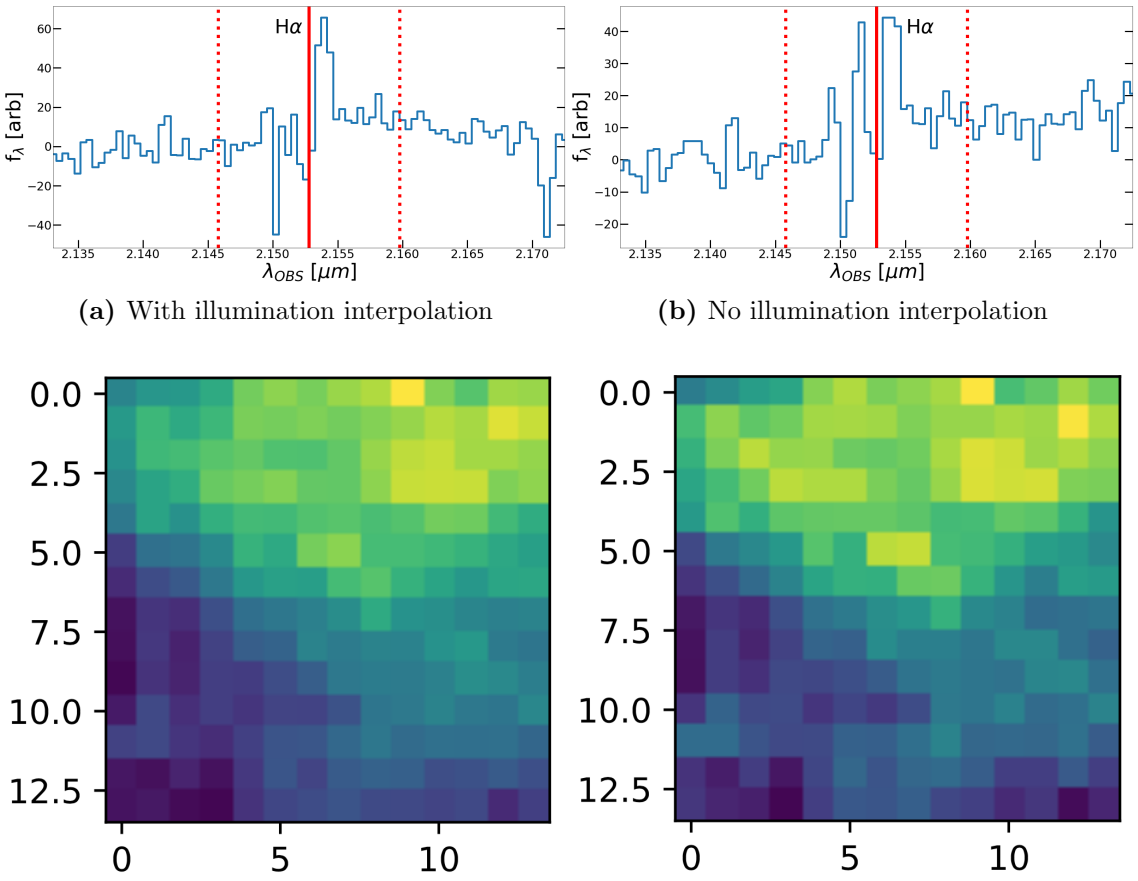

(a) With illumination interpolation

(b) No illumination interpolation

Figure 3.7: Comparison of the spectra, in correspondence of the expected Hα emission line, obtained performing the illumination correction with the interpolation of the six flat fields (left) and without the interpolation (right). 2D images are obtained by summing spaxels over the wavelength range between red dotted lines shown in the 1D spectra. The red vertical line represents the expected Hα emission line position.

3.5 Line Detection

We measured the emission line flux, FWHM, and redshift by fitting three Gaussians to the H-band part of spectra for Hβ, [OIII]λ4960.30 and [OIII]λ5008.24 and two Gaussians in the K-band part of spectra for Hα and [NII]λ6585.23. [NII] is a doublet with the two emission lines at 6549.86$\mathring{A}$ and 6585.23$\mathring{A}$, the theoretical flux ratio is

$$\frac{f_{[NII]\lambda 6585.23}}{f_{[NII]\lambda 6549.86}} \simeq 3. \tag{3.2}$$

Since the [NII] line amplitude is comparable to the noise level of our spectra, it is difficult to constrain its properties from these fits and we focus only on the most energetic line of the [NII] doublet. Therefore, we fix the [NII]λ6585.23 redshift and FWHM to be the same as Hα as no other strong emission line is available in the K-band spectral range, while leaving its flux as a free parameter. Similarly, the redshift and FWHM of [OIII]λ4960.30 lines are fixed to those of [OIII]λ5008.24. We furthermore impose a constraint on the [OIII]λ4960.30 flux such that the ratio of [OIII]λ5008.24/[OIII]λ4960.30 is equal to the

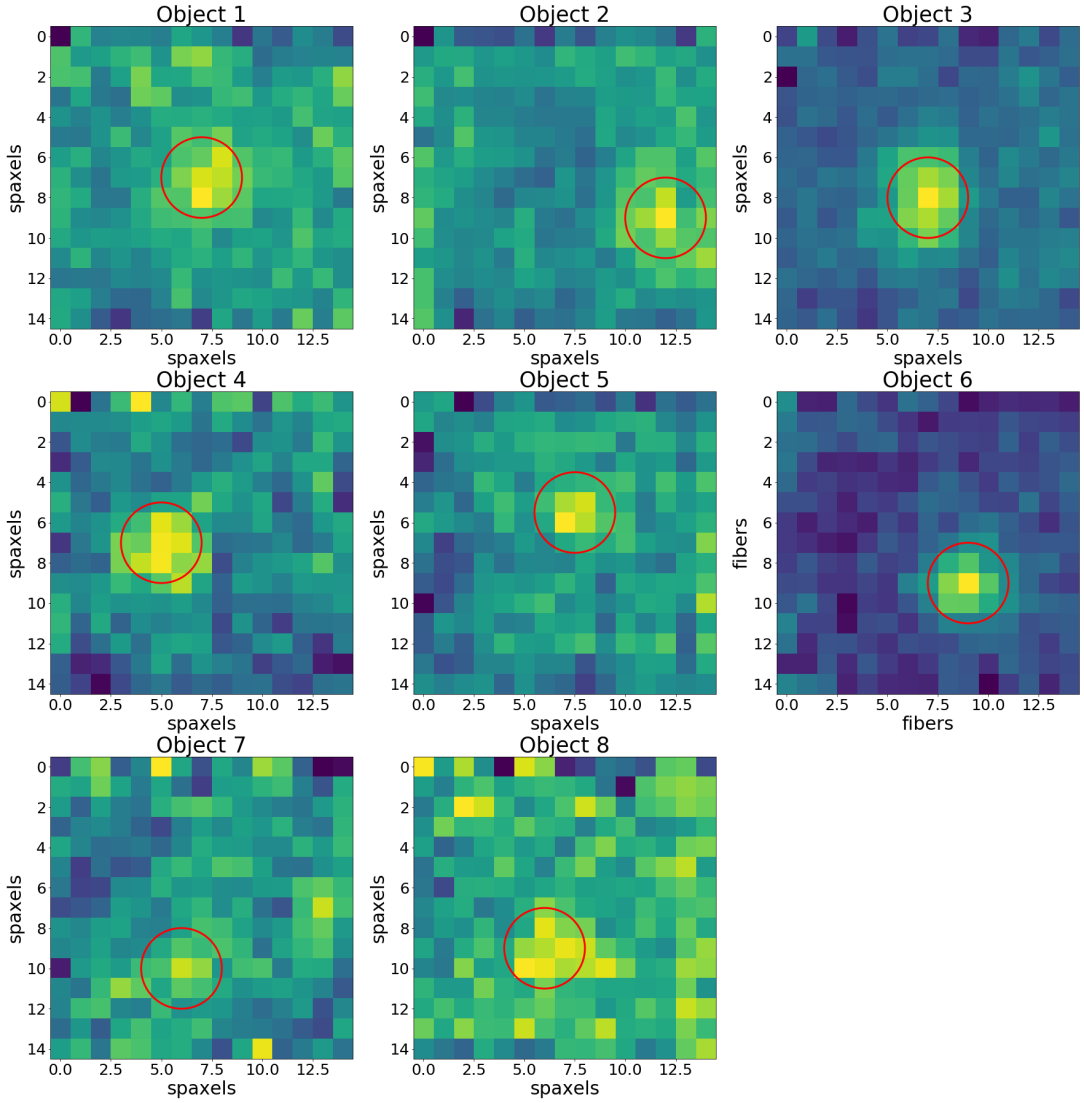

Figure 3.8: The [OIII] images for the eight LAEs detected. The diameter of the red circles is 0.7″, the FWHM of the Gaussian model used in the spectra extraction

theoretical value of 2.98. We detected Hβ leaving free all Gaussian parameters for Object 1. For all the others Objects we fix its redshift and FWHM from [OIII]λ5008.24. All line fluxes are constrained to be positive. The uncertainties for line flux, FWHM, and redshift were quantified as the 68% confidence interval from 10^3 Monte Carlo realizations of the data, where the input spectrum is given as the observed spectrum perturbed by Gaussian random noise, with the Gaussian σ equal to the noise spectrum value at a given wavelength. Imposing a 5σ detection limit over the 8 LAEs that we detect 1 Hβ, 7 [OIII]λ4960.30, 7 [OIII]λ5008.24 and 6 Hα. Two objects are detected in Hβ with more than 3σ significance and one in [NII]. For one LAE was impossible to detect any emission line with significance because of the presence of strong sky emission lines in correspondence of all 5 emission lines studied. We associate a redshift $\left(z = \frac{\lambda_{obs} - \lambda_{rest}}{\lambda_{rest}}\right)$ and its error $\left(\sigma_z = \frac{\sigma_{\lambda_{obs}}}{\lambda_{rest}}\right)$ to every line detected with the wavelength as a free parameter. The systemic redshift of every LAE is a weight average on the redshift from these lines.

3.5.1 Upper limit on Hβ and [NII] flux

A robust measurement of the [NII] line fluxes is critical to constrain the metallicities of our sample. As only one of our eight LAEs has a detected [NII] line, we quantified the upper limits via simulations, inserting a mock line at the [NII] wavelength with varying flux and fixing the line FWHM to that of the Hα line. We measure the SNR of the mock line by performing the same fitting procedure, using Monte Carlo realizations of data, described in the previous section. The 1σ upper limit is estimated as one fifth of the input flux which has a SNR of 5. In this way we measured the [NII] 1σ upper limit for 5 LAEs. For one LAE is possible to determine the Hβ flux upper limit using the same procedure. In other two cases it was impossible to measure the flux upper limit for Hβ because of the overlapping residuals of the sky subtraction. For these two LAEs we estimate the Hβ upper limit flux assuming the ratio of Hα/Hβ to be equal to the theoretical value with no dust extinction of 2.85. Figure 3.10 and Figure 3.9 show the final H and K-band spectra with the line detected. Table 3.1 summarizes the measured emission line wavelength, flux or flux upper limit and redshift.

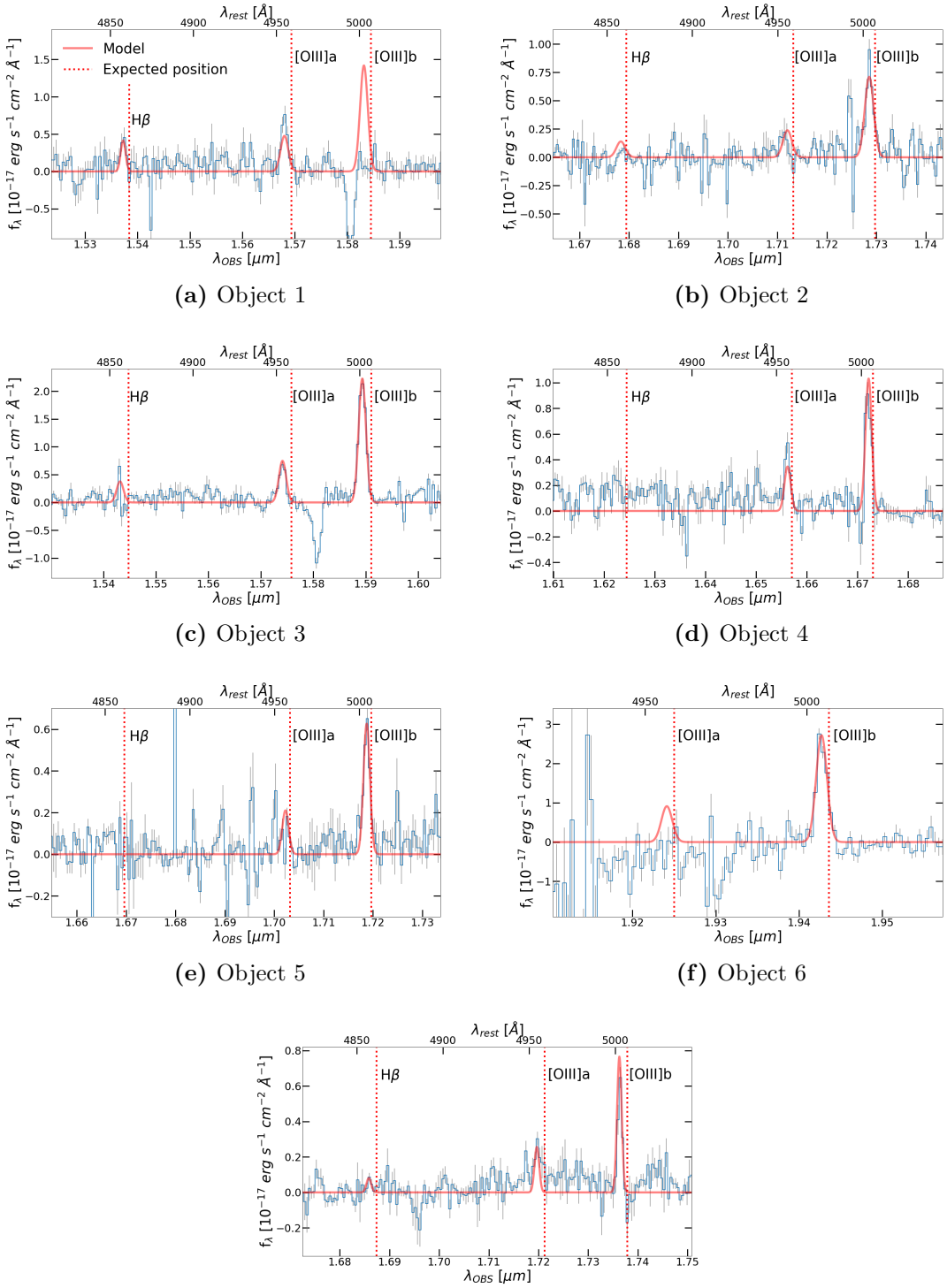

(a) Object 1 **(b)** Object 2

(c) Object 3 **(d)** Object 4

(e) Object 5 **(f)** Object 6

(g) Object 8

Figure 3.9: *H*-band spectra around [OIII]$\lambda\lambda$4960.30, 5008.24 and Hβ for the 7 [OIII]λ5008.24 detected LAEs. The best-fit triple Gaussian is overplotted in red. Vertical dotted lines are the expected wavelengths of Hβ, [OIII]$\lambda\lambda$4960.30, 5008.24, these expected line wavelengths are calculated using the redshift from the HETDEX catalog.

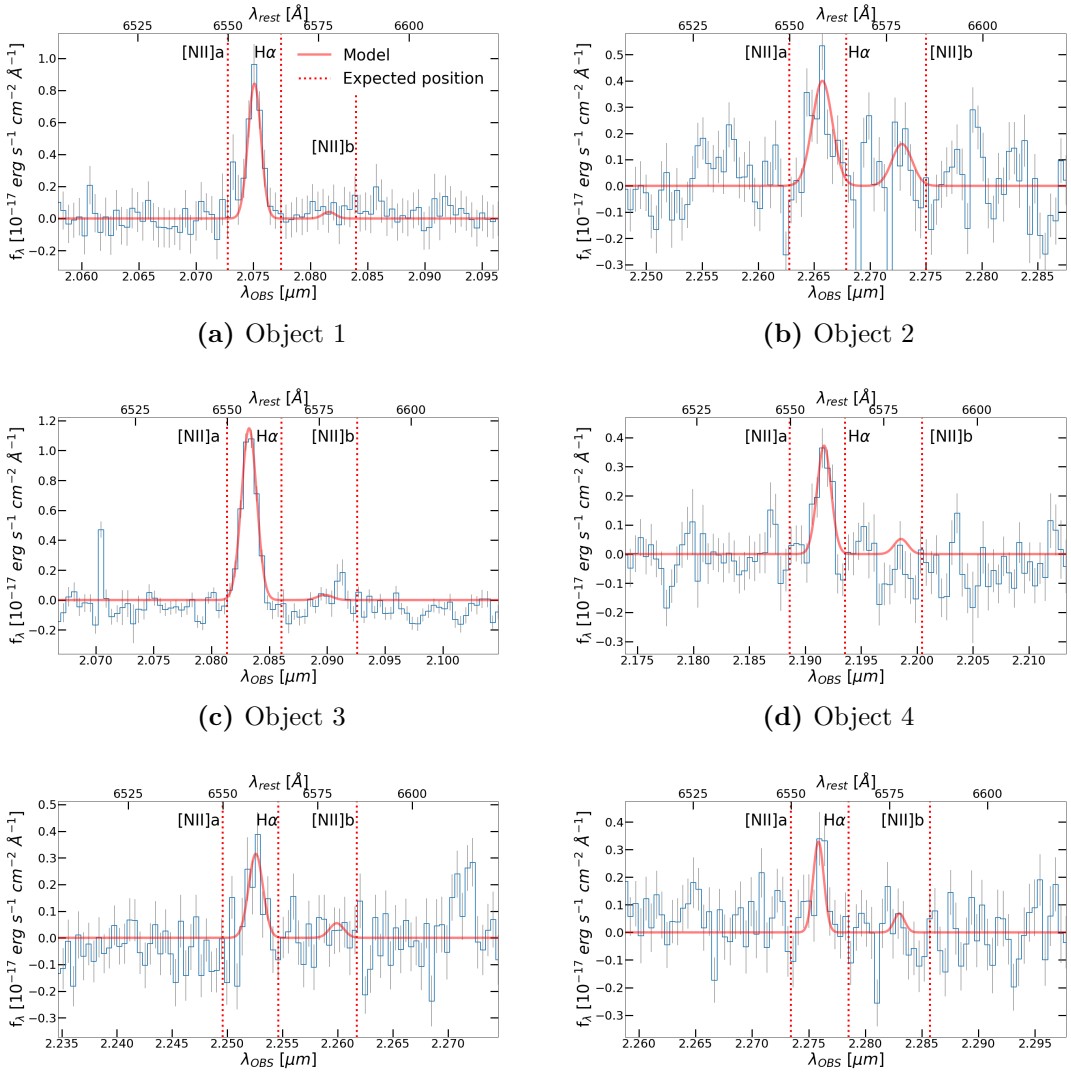

(a) Object 1 **(b)** Object 2

(c) Object 3 **(d)** Object 4

(e) Object 5 **(f)** Object 8

Figure 3.10: K-band spectra around Hα and [NII]λ6585.23 for the 6 Hα detected LAEs. The best-fit double Gaussian is overplotted in red. Vertical dotted lines are the expected wavelengths of [NII]λ6549.86, Hα, [NII]λ6585.23, these expected line wavelengths are calculated using the redshift from the HETDEX catalog.

Table 3.1: Emission line detections

Object	Line	λ_{rest} (Å)	F_{line} (10^{-17} erg s^{-1} cm^{-2})	SNR	z
1	Hβ	4862.68	4.85 ± 0.47	10.2	2.16131 ± 0.00015
	[OIII]	5008.24	31.15 ± 1.93	16.2	2.16111 ± 0.00008
	Hα	6564.61	13.04 ± 0.72	18.1	2.16106 ± 0.00006
	[NII]	6585.23	< 2.02	–	
					($z_{sys} = 2.16110 \pm 0.00004$)
2	Hβ	4862.68	< 3.14	–	
	[OIII]	5008.24	15.99 ± 1.43	11.1	2.45146 ± 0.00014
	Hα	6564.61	8.99 ± 1.16	7.8	
	[NII]	6585.23	3.59 ± 1.14	3.2	
					($z_{sys} = 2.45146 \pm 0.00014$)
3	Hβ	4862.68	6.20 ± 1.89	3.3	
	[OIII]	5008.24	38.98 ± 1.19	32.8	2.17346 ± 0.00004
	Hα	6564.61	18.91 ± 0.75	25.2	2.17346 ± 0.00004
	[NII]	6585.23	< 0.57	–	
					($z_{sys} = 2.17346 \pm 0.00003$)
4	Hβ	4862.68	< 2.03	–	
	[OIII]	5008.24	16.08 ± 1.02	15.8	2.33891 ± 0.00017
	Hα	6564.61	5.81 ± 0.80	7.27	2.33862 ± 0.00018
	[NII]	6585.23	< 0.81	–	
					($z_{sys} = 2.33878 \pm 0.00012$)
5	Hβ	4862.68	< 1.80	–	
	[OIII]	5008.24	10.25 ± 0.90	11.4	2.43179 ± 0.00015
	Hα	6564.61	5.15 ± 0.80	5.2	2.43140 ± 0.00023
	[NII]	6585.23	< 0.90	–	
					($z_{sys} = 2.43168 \pm 0.00012$)
6	[OIII]	5008.24	44.58 ± 1.81	24.6	2.87903 ± 0.00006
					($z_{sys} = 2.87903 \pm 0.00006$)
8	Hβ	4862.68	$0.96 \pm 0,24$	3.97	
	[OIII]	5008.24	9.05 ± 0.67	13.5	2.46687 ± 0.00012
	Hα	6564.61	3.89 ± 0.84	4.6	
	[NII]	6585.23	< 0.81	–	
					($z_{sys} = 2.46687 \pm 0.00012$)

Dash bars mean non-detection, while blank fields indicate non-independent quantities: redshifts of [NII] and of Hβ with SNR lower than 5 are fixed to that of [OIII]λ5008.24 or Hα. [OIII]λ4960.30 is not reported because its redshift is fixed to that of [OIII]λ5008.24 and its flux is determined by the theoretical value $f([\text{OIII}]\lambda5008.24)/f([\text{OIII}]\lambda4960.30) = 2.98$.

Chapter 4

KMOS^{3D}

KMOS^{3D} (Wisnioski et al., 2019) is an integral field spectroscopic survey of 739 galaxies at $0.6 < z < 2.7$ using KMOS. KMOS^{3D} mapped the ionized gas distribution and kinematics of galaxies on and off the star-forming main sequence through the Hα, [NII] and [SII] emission lines. The targets were drawn from the 3D-HST survey at $0.7 < z < 2.7$, $\log(M_\star/M_\odot) > 9$ and $K < 23$ mag, with the requirement of having an accurate redshift and the lines of interest falling away from telluric emission lines and low transmission spectral regions. No explicit criterion involving AGN activity was applied in the targets selection. Among the sample of 739 target galaxies, 581 are detected in Hα. These galaxies span $0.6 < z < 2.7$ and $9.0 < \log(M_\star/M_\odot) < 11.7$. KMOS^{3D} and HETDEX have both detections in the COSMOS field in the redshift range $1.9 < z < 2.7$. In the KMOS^{3D} catalog a precise measure of the systemic redshift, from Hα, is available. We match these two catalogs to add LAEs to the sample studied in this work. We perform the catalog match by asking the angular separation to be smaller than $2''$ and $|z_{\mathrm{Ly}\alpha} - z_{sys}| \leq 0.1$ that corresponds to a Lyα velocity offset of $\Delta v_{\mathrm{Ly}\alpha} \leq 1000$ km s^{-1} at $z \sim 2.3$. Using these constrains we find three sources in common between KMOS^{3D} and HETDEX catalogs. We add these three LAEs to the sample that we obtained from our KMOS observations. Because of their lower Lyα fluxes these three LAEs weren't selected for observations from the HETDEX catalog, they have consequently larger errors in their Lyα line parameters. Figure 4.1 shows in the I-band and in the Ks-band the objects present in KMOS^{3D} and in HETDEX. In Figure 4.2 are shown the Lyα emission of these three LAEs. Table 4.1 summarizes the measured Lyα flux and redshift from the HETDEX catalog. Hα properties are in Table 4.2.

Table 4.1: Lyα line properties

Object	$F_{\mathrm{Ly}\alpha}$ (10^{-17} erg s^{-1} cm^{-2})	$z_{\mathrm{Ly}\alpha}$
COS4 10347	24.29 ± 4.06	2.0177 ± 0.0005
COS4 11363	22.73 ± 4.77	2.1010 ± 0.0009
COS4 12148	52.90 ± 11.74	2.4626 ± 0.0009

Lyα line properties from the HETDEX catalog for the three KMOS^{3D} LAEs.

Table 4.2: Hα properties from KMOS^{3D}

Object	$F_{\mathrm{H}\alpha}$ (10^{-17} erg s^{-1} cm^{-2})	SNR	$z_{\mathrm{H}\alpha}$
COS4 10347	13.11 ± 0.90	14.6	2.06329 ± 0.00005
COS4 11363	10.00 ± 0.32	31.3	2.09625 ± 0.00016
COS4 12148	13.55 ± 1.11	12.2	2.46018 ± 0.00006

Hα line properties from the KMOS^{3D} catalog for the three LAEs present in the HETDEX survey too.

4.1 COS4 10347

COS4 10347 is of particular interest because is the only LAE of our sample for which the systemic redshift is larger than the redshift from the Lyα line. This means that the Lyα line is blueshifted compared to systemic emission lines. We found no X-ray point like source counterpart for this object in the *Chandra COSMOS-Legacy* Survey (Marchesi et al., 2016), the deepest Chandra catalog on the COSMOS field. We use the online CSTACK tool[1] to measure its mean X-ray flux by an X-ray stacking analysis based on the *Chandra COSMOS-Legacy* Survey datasets. We find no associated X-ray detection in the 0.5-2 keV and 2-8 keV bands. COS4 10347 Lyα and Hα fluxes and $\mathrm{EW}_{\mathrm{Ly}\alpha}$ lower limit are comparable to fluxes and $\mathrm{EW}_{\mathrm{Ly}\alpha}$ of the other two sources. Figure 4.1 shows that this source has an optical counterpart fainter than the other two sources but there's no difference by eye between the COS4 10347 infrared image and the one of other sources. We exclude this LAE from the study between the Lyα velocity offset and the other physical parameters. In Chapter 5 we measure the physical properties of this source trying to understand the cause of the Lyα blueshift.

[1] http://lambic.astrosen.unam.mx/cstack/

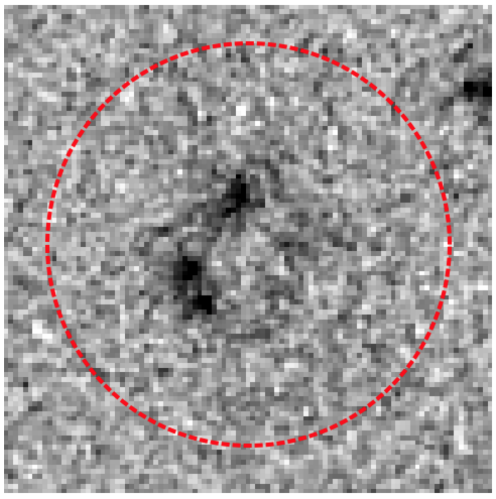

(a) COS10347 HST F814W - $3'' \times 3''$

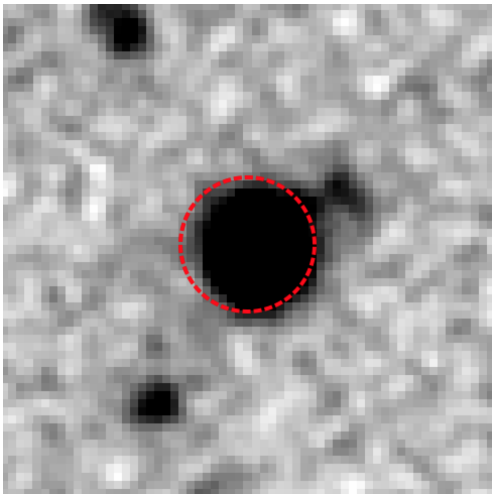

(b) COS10347 UVISTA Ks - $9'' \times 9''$

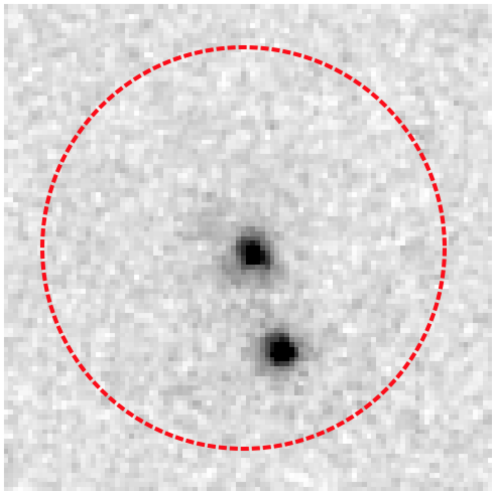

(c) COS11363 HST F814W - $3'' \times 3''$

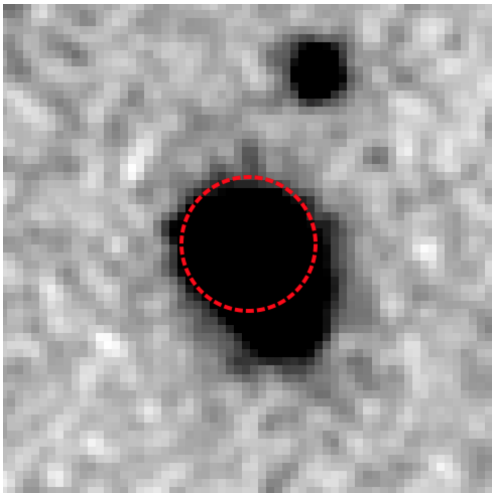

(d) COS11363 UVISTA Ks - $9'' \times 9''$

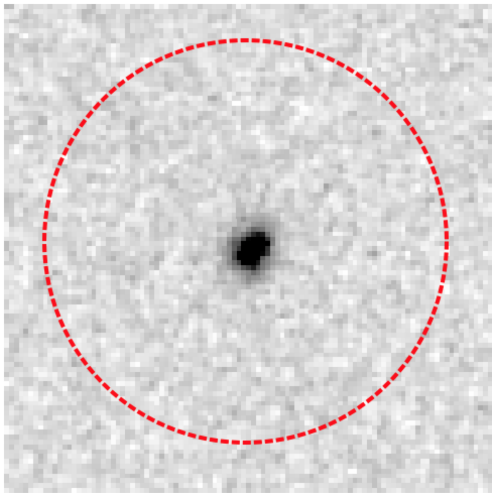

(e) COS12148 HST F814W - $3'' \times 3''$

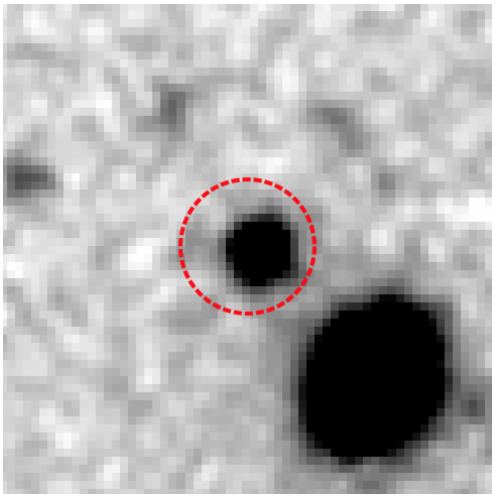

(f) COS12148 UVISTA Ks - $9'' \times 9''$

Figure 4.1: Cutout stamp images of the three LAEs present in KMOS3D and HETDEX catalogs. On the left $3'' \times 3''$ images from $HST/F814W(I)$. On the right $9'' \times 9''$ images from VISTA Ks. Red dotted circles have a $2.5''$ diameter and are centered.

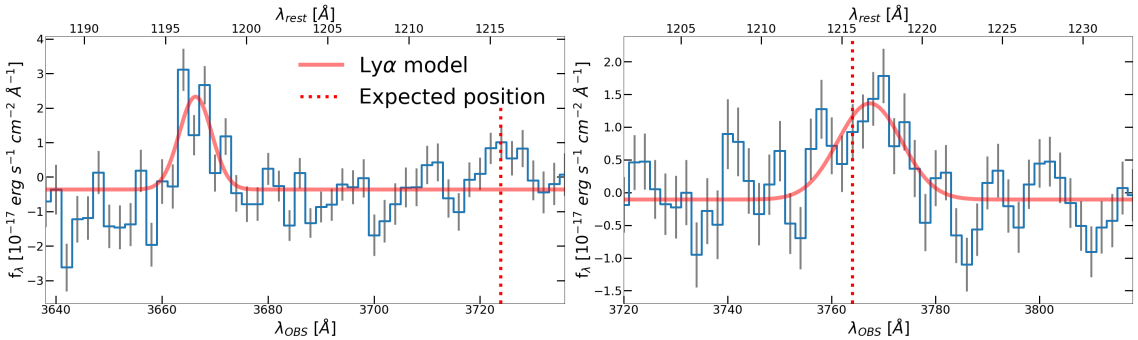

(a) COS4 10347 **(b)** COS4 11363

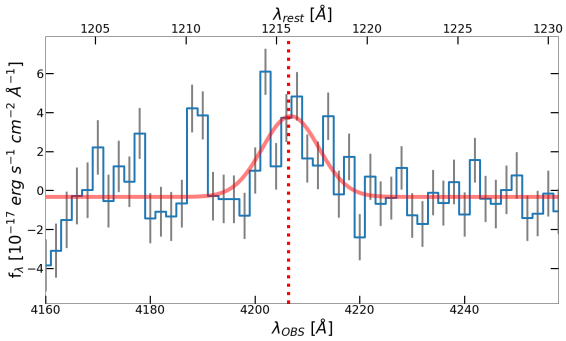

(c) COS4 12148

Figure 4.2: HETDEX spectra around Lyα for the 3 LAEs present in the first HETDEX data release and KMOS^{3D} catalog. The best-fit single Gaussian is overplotted in red. The red dotted vertical line is the expected Lyα wavelength from the systemic redshift. Every exposure was corrected for the heliocentric velocity and wavelength converted from air to vacuum wavelength.

Chapter 5

Physical Properties

5.1 Lyα Velocity Offset

We measure the difference between the redshift of Lyα from HETDEX catalog and the systemic redshift computed in Section 3.5. To calculate the Lyα velocity offset properly we correct every HETDEX data used for Earth's motiond during the observation. We utilize the task `barycorr` from Wright & Eastman (2014) to calculate the radial heliocentric velocity of the observer with respect to the heliocentric frame, v_{helio}, for each exposure. Using the median time of the observation, we find v_{helio} to range between $[-2.0, +29.8]$ km s^{-1}. We correct wavelengths for HETDEX spectra by

$$\lambda_{helio} = \lambda_{mis} \left(1 + \frac{v_{helio}}{c}\right), \tag{5.1}$$

where $c = 299792.458$ km s^{-1} is the speed of light. HETDEX spectra are calibrated using air wavelength, we convert them to vacuum wavelength because KMOS spectra are calibrated in vacuum wavelength. As described in Section 2.1 we use the relation from Morton (2000) to convert the HETDEX spectra from air to vacuum wavelength. The systemic redshift for each object is calculated as the weighted mean of the redshifts from lines detected with the line position as a free parameter. For the LAEs from the KMOS^3D catalog the systemic redshift is measured only using the observed wavelength of Hα because is the only emission line available in the catalog. To derive the Lyα velocity offset we first correct the observed Lyα wavelength for the systemic redshift and than measure the velocity difference from the $\lambda_{\mathrm{Ly}\alpha}$ rest frame value:

$$\Delta v_{\mathrm{Ly}\alpha} = \left(\frac{\lambda_{\mathrm{Ly}\alpha - obs}}{(1 + z_{sys})\lambda_{\mathrm{Ly}\alpha}} - 1\right) c \tag{5.2}$$

Figure 5.1 shows the histogram of Lyα velocity offsets compiled for LAEs from this work and from Song et al. (2014) (S14). For our whole sample we obtain Lyα velocity offsets ranging from 123 km s^{-1} to 372 km s^{-1}, with an average $\Delta v_{\mathrm{Ly}\alpha} = 273$ km s^{-1}. This value is comparable with S14 average Lyα velocity offset, considering also measures from S14 we measure an average Lyα velocity offset of 233 km s^{-1}. COS4 10347 is the only target with a negative Lyα velocity offset, for this we measure $\Delta v_{\mathrm{Ly}\alpha} = -4543$ km m^{-1}.

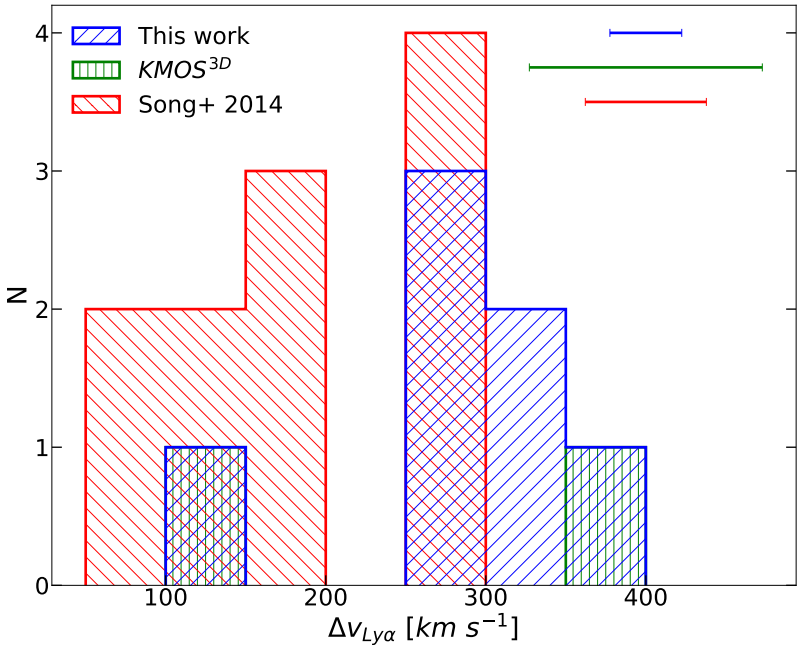

Figure 5.1: Compilation of Lyα velocity offsets for 20 LEAs at $z = 2 - 2.5$, 9 from this study (matching of $KMOS^{3d}$ and HETDEX catalog) and 11 from S14, of which Lyα velocity offsets are measured from the centroids of Lyα and nebular (Hα and/or [OIII]) lines, where the latter represent the systemic redshift of these galaxies. On the upper right corner are shown the typical uncertainties in velocity offsets for the three samples.

5.2 Stellar Mass

The COSMOS2015 catalog (Laigle et al., 2016) contains photometric redshifts and stellar masses for more than half a million objects ($1 < z < 6$) over the 2deg^2 COSMOS field. This catalog includes Y J H K_S images from the UltraVISTA-DR2 survey, Y-band from Subaru/Hyper-Suprime-Cam and infrared data from the Spitzer Large Area Survey with the Hyper-Suprime-Cam *Spitzer* legacy program. They derive photometric redshifts and stellar masses using the LEPHARE SED fitting code (Ilbert et al., 2006). To compute the photometric redshift the code performs the χ^2 analysis between the fluxes predicted by the templates and the observed fluxes of each galaxy. They derive the galaxy stellar masses using a library of synthetic spectra generated using the Stellar Population Synthesis (SPS) model of Bruzual & Charlot (2003), assuming a Chabrier (2003) Initial Mass Function (IMF) and an exponentially delayed Star Formation History (SFH) ($\tau^{-2}te^{-t/\tau}$). Through a comparison with the zCOSMOS bright spectroscopic redshift, they estimate the precision of the photometric redshift using the normalized median absolute deviation (NMAD) (Hoaglin et al., 1983) finding as $\sigma_{\Delta z/(1+z_s)} = 1.48\times$ median$(|z_p - z_s|/(1 + z_s)) = 0.007$. A precise redshift measurement is fundamental to perform a matching with galaxies from our KMOS observations. By matching our seven LAEs, with at least one emission line detected in KMOS observation, with the COSMOS2015 catalog we find six galaxies in common. For these the COSMOS2015 catalog lists a stellar mass and a SFR measure.

Table 5.1 summarizes the stellar mass, SFR, age and χ^2 from the SED fitting.
The KMOS^{3D} catalog contains stellar masses and a star formation rates (SFR) for the three LEAs we selected from this catalog. They measure the SFR (Wisnioski et al., 2019) using the Hα relation from Kennicutt (1998), the stellar masses are measured from a SED fitting (Momcheva et al., 2016). Table 5.2 shows the stellar mass and SFR for the three LAEs from KMOS^{3D}. KMOS^{3D} galaxies have and average stellar mass of 5×10^{10} $M_\odot$, more than an order of magnitude larger than the average stellar mass LAEs from KMOS observations ($\langle M_* \rangle = 1 \times 10^9$ $M_\odot$). COS4 10347 stellar mass is comparable to the stellar mass of other KMOS^{3D} LAEs.

Table 5.1: SED Fitting Results

Object	log Stellar Mass ($M_\odot$)	SFR ($M_\odot yr^{-1}$)	log Age (yr)	χ^2_r
1	$9.80^{+0.04}_{-0.07}$	$50.2^{+8.5}_{-7.3}$	8.2	4.6
2	$8.27^{+0.08}_{-0.07}$	$4.0^{+0.7}_{-0.6}$	8.1	2.7
3	$9.52^{+0.05}_{-0.06}$	$35.7^{+7.9}_{-6.4}$	8.1	4.4
5	$8.72^{+0.11}_{-0.12}$	$3.1^{+0.6}_{-0.5}$	8.8	1.7
6	$9.62^{+0.06}_{-0.06}$	59^{+12}_{-9}	8.2	2.6
8	$8.79^{+0.04}_{-0.04}$	$15.7^{+3.0}_{-2.4}$	8.0	4.1

Physical properties from the COSMOS2015 catalog.

Table 5.2: KMOS^{3D} Properties

Object	log Stellar Mass ($M_\odot$)	SFR ($M_\odot yr^{-1}$)	log Age (yr)
COS4 10347	10.76	135	8.5
COS4 11363	11.28	436	8.8
COS4 12148	10.22	92	8.4

Physical properties from the KMOS^{3D} catalog.

5.3 Dust Extinction and Galactic Extinction

We measure the dust extinction to extract the intrinsic luminosities, L_{int}. In this work we use the empirical extinction relation found in Calzetti et al. (1994),

$$L_{int}(\lambda) = L_{obs}(\lambda)10^{0.4A_\lambda} = L_{obs}(\lambda)10^{0.4k(\lambda)E(B-V)} \tag{5.3}$$

where L_{obs} is the observed luminosity, A_λ is the extinction at the wavelength λ and $k(\lambda)$ the reddening curve. We use the reddening curve found in Calzetti et al. (2000). The color excess $E(B-V)$ is defined by,

$$E(B-V) = (B-V)_{obs} - (B-V)_{int} \tag{5.4}$$

which is the change in the $(B-V)$ color due to dust attenuation. For lines available in our observations we derive dust extinction from Balmer decrements using the following relation from Dominguez et al. (2013):

$$E(B-V) = \frac{E(\mathrm{H}\beta - \mathrm{H}\alpha)}{k(\lambda_{\mathrm{H}\beta}) - k(\lambda_{\mathrm{H}\alpha})} = \frac{2.5}{k(\lambda_{\mathrm{H}\beta}) - k(\lambda_{\mathrm{H}\alpha})} \log_{10}\left[\frac{(\mathrm{H}\alpha/\mathrm{H}\beta)_{obs}}{(\mathrm{H}\alpha/\mathrm{H}\beta)_{int}}\right] \tag{5.5}$$

where $k(\lambda_{\mathrm{H}\beta})$ and $k(\lambda_{\mathrm{H}\alpha})$ are the values of the reddening curve evaluated at Hβ and Hα wavelengths, respectively. The factor $E(\mathrm{H}\beta - \mathrm{H}\alpha)$ is analogous to the color excess but defined for Hβ and Hα instead of the B and V-bands. The intrinsic Balmer decrement, $(\mathrm{H}\alpha/\mathrm{H}\beta)_{int}$, remains roughly constant for typical gas conditions in star-forming galaxies. We assume the value of $(\mathrm{H}\alpha/\mathrm{H}\beta)_{int} = 2.86$, corresponding to a temperature $T = 10^4$ K and an electron density $n_e = 10^2$ cm^{-3} for Case B recombination Osterbrock (1989), this choice is standard for star-forming galaxies in the literature. With these assumptions we calculate the nebular color excess with the following equation,

$$E(B-V) = 1.97 \log_{10}\left[\frac{(\mathrm{H}\alpha/\mathrm{H}\beta)_{obs}}{2.86}\right]. \tag{5.6}$$

We calculate the color excess, using Equation 5.6, for the three LAEs with a $> 3\sigma$ Hβ detection. Their color excess ranges from a null color excess to $E(B-V) = 0.30$. For Object 2 we have only a 1σ Hβ upper limit detection, for this object we calculate a color excess lower limit that is compatible with no dust extinction. For Objects 4 and 5 in Section 3.5 we determined the Hβ upper limit using the same conditions of Case B recombination Osterbrock (1989) and assuming no dust absorption. For LAEs from the KMOS^{3D} catalog is not possible to measure the color excess with this method because Hβ detections are not available. In S14 they derived the color excess from a SED fitting and we have to take account of this in the next Chapter comparing results from their and our work. We correct emission line fluxes for the galactic extinction, this correction depends on the sky position of the target and from the observing band. The COSMOS field is very little affected by this effect and the correction is constant over the entire range. We perfom the correction the equation:

$$f_{gal-corr} = \frac{f_{obs}}{10^{-\frac{A_\lambda}{2.5}}} \tag{5.7}$$

where A_λ is the total absorption in mags, it is 0.009 in the H-band and 0.006 in the K-band, this correspond respectively to a correction factor of 0.992 and 0.994.

5.4 Gas-phase Metallicity

Using the N2 index of Pettini & Pagel (2004) we can calculate the metallicity of Object 2, indeed it is the only object that has a 3σ [NII]λ6585.23 detection. For the other five LEAs with a [NII]λ6585.23 upper limit we can place constrains on the gas phase metallicity using the same relation. The metallicity, oxygen abundance, is given by,

$$12 + \log(O/H) = 8.90 + 0.57 \times N2 \tag{5.8}$$

$$N2 \equiv \log\left(\frac{[NII]\lambda 6585.23}{\mathrm{H}\alpha}\right) \tag{5.9}$$

The estimated 1σ metallicity upper limit ranges from $12 + \log(O/H) = 8.03$ to 8.51 (in solar metallicity 0.21 $\mathrm{Z}_\odot$ - 0.65 $\mathrm{Z}_\odot$), with an average upper limit of 8.37 (0.47 $\mathrm{Z}_\odot$), for Object 2 we measure $12 + \log(O/H) = 8.67 \pm 0.09$ ($0.93^{+0.21}_{-0.17}$ $\mathrm{Z}_\odot$). For LAEs from the KMOS^{3D} catalog is not possible to measure the gas-phase metallicity with the N2 index because the [NII]λ6585.23 line is not available.

5.5 AGN contamination

Gas-phase metallicity measured from emission lines is reliable only for star-forming galaxies, the eventual presence of an active galactic nucleus (AGN) would make this measures unreliable, because the AGN ionizing spectra are quite different from those in star-forming regions. Further we are interested in investigating the mechanism that drives the gas outflow and the consequent Lyα line presence. One possible candidate is the presence of an AGN in the host galaxy. We search for X-ray point sources counterparts of our objects in the catalog from Marchesi et al. (2016). This catalog contains optical and infrared counterparts of the *Chandra COSMOS-Legacy* Survey, the deepest Chandra catalog on the COSMOS field. By cross-matching our sources with this catalog we don't find any object in common. Since our objects are not resolved X-ray sources themselves we use the CSTACK tool to measure their mean X-ray flux by an X-ray stacking analysis based on the *Chandra COSMOS-Legacy* Survey datasets. We find no associated X-ray detection, down to a flux limit of 1.1×10^{-15} erg s^{-1} cm^{-2} in the 2-8 keV band. Then we search for the presence of AGN in our sample using the BPT diagram (Baldwin et al., 1981). This diagnostic diagram is based on optical emission lines that we detected in our KMOS observations. For the two LAEs from the KMOS^{3D} catalog we can't perform this test because only Hα is available. Figure 5.2 shows our objects have elevated [OIII]λ5008.24/Hβ ratio compared to star-forming galaxies in local Universe, the dashed line represents the boundary between pure star-forming galaxies and star-forming/AGN composites at $z \sim 0.1$ (Kewley et al., 2001). This elevated [OIII]λ5008.24/Hβ ratio has been reported by several studies for some LBGs at high redshift and also for local starbusts with no indication of AGN. We conclude that while we can't exclude the presence of low-luminosity AGNs which could be obscured or undetected, there are no confirmed AGNs in our sample.

5.6 Star Formation Rate

KMOS^{3D} galaxies have a SFR measurement from their catalog as described in Section 5.2.

For LAEs observed with KMOS we can compute the SFR using different methods. For the four objects present in the COSMOS2015 catalog we have a SFR measure from UV and IR luminosities. This sample is characterized by a mean SFR value of 23 M$_\odot$ yr^{-1}, ranging between 3 and 50 M$_\odot$ yr^{-1}. This is comparable to the average SFR value ($\langle SFR_{SED} \rangle = 35$ M$_\odot$ yr^{-1}) inferred from SED fitting for narrowband selected LAEs in Guaita et al. (2011). We can derive SFRs directly from our KMOS observations, assuming a Salpeter initial mass function (IMF) and solar metallicity, using the relation from Kennicutt (1998):

$$SFR(\mathrm{H}\alpha) \ \left(\mathrm{M}_\odot \ \mathrm{yr}^{-1}\right) = 7.9 \times 10^{-42} \ L(\mathrm{H}\alpha)_{corr}. \tag{5.10}$$

To use this relation we convert Hα fluxes to Hα luminosities as

$$L(\mathrm{H}\alpha)_{corr} = f(\mathrm{H}\alpha)_{obs} \times 10^{0.4E(B-V)k(\lambda_{\mathrm{H}\alpha})} \times 4\pi D_L^2 \tag{5.11}$$

where $k(\lambda)$ is the Calzetti extinction curve and D_L is the luminosity distance extracted for the systemic redshift. For Objects 1, 3 and 8, the only galaxies with an available measure of the color excess, we measure an average SFR$_{\mathrm{H}\alpha}$ of 43 M$_\odot$ yr^{-1} ranging from 31 to 62 M$_\odot$ yr^{-1}. For Object 2 we compute a SFR$_{\mathrm{H}\alpha}$ lower limit using the color excess lower limit measured in Section 5.3. For Objects 4 and 5 no Hβ detections are available, we determine a SFR$_{\mathrm{H}\alpha}$ lower limit assuming no dust extinction. To have a comparison for

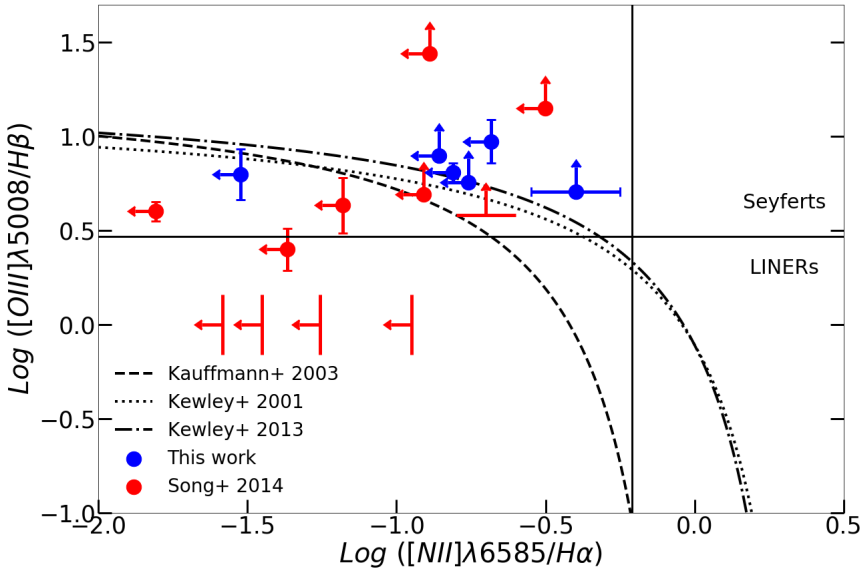

Figure 5.2: The BPT emission line diagnostic diagram. Blue dots are our $z = 2 - 2.5$ LAEs and red from S14. Arrows denote 1σ limits for objects for which at least one emission line is unavailable (either not observed or undetected). The black dashed curve represents the boundary between pure star-forming galaxies and star-forming/AGN composites from Kauffmann et al. (2003), and the black dotted and dash-dotted curves are the maximum star-burst from Kewley et al. (2001) and its updated version at $z \sim 2.5$ (Kewley et al., 2013), respectively.

$SFR_{H\alpha}$ of similar objects we measure it for the three LAEs from S14 with Hα and Hβ detected, here we measure the color excess from Eq. 5.6. We calculate an average $SFR_{H\alpha}$ of 38 $M_\odot$ yr^{-1}, this value is comparable to the mean $SFR_{H\alpha}$ of our KMOS galaxies. In S14 is available a measure of the color excess from a SED fitting, this is more accurate than the value from Eq. 5.6 because Hα fluxes can be affected by internal dust extinctions assuming the ionized gas suffers a greater extinction as suggested by Calzetti et al. (2000). This would lead to a underestimation of the SFR using E(B-V) from Eq. 5.6. Indeed for the same three LAEs of S14, using Eq. 5.10 but correcting Hα luminosity with E(B-V) from the SED fitting, they measure a mean SFR of 101 $M_\odot$ yr^{-1} instead of 38 $M_\odot$ yr^{-1}. SFR from Hα is an indiactor of the instantaneous SFR because Hα emission line is produced in the HII regions. The SFR from a SED fitting, as it is from COSMOS2015 catalog, probe the average SFR over the past ~ 100 Myr. The SFRs we measure from the Hα luminosity are systematically higher than these from the COSMOS2015 catalog, this suggest an increasing of the SFR for our targets.

5.7 Lyα Equivalent Width

LAEs have faint continuum emission level, this makes impossible to measure the equivalent width (EW) of emission lines only from spectroscopy. For this reason we determine the continuum flux by using the broad-band flux near the Lyα line. This is possible for the four LAEs present in COSMOS2015 catalog with avalable flux measurements. For our LAEs

Lyα is observed at $\sim 4000\mathring{A}$ and the continuum can be extracted from Subaru Suprime-Cam photometric measurements in the IA427 band that are present in the catalog. In this way we measure the continuum flux density for Objects 1, 2, 3 and 5. These have an average continuum flux density of $\langle f_{cont-phot} \rangle = 0.13 \times 10^{-17}$erg cm^{-2} s^{-1} $\mathring{A}^{-1}$. From these we extract the rest-frame Lyα EW by using fluxes and redshifts in Table 2.1 and we have an average $\langle EW_{\mathrm{Ly}\alpha-phot} \rangle = 63\mathring{A}$ ranging from 44 $\mathring{A}$ to 87 $\mathring{A}$. We than measure a rest-frame Lyα EW lower limit using spectroscopy for LAEs from our sample. We can't perform this measure on the two objects from KMOS^{3D} because is not possible extract the continuum flux density from their spectra. We extract the continuum flux density upper limit from the best-fit model in a $\Delta\lambda_{rest} = 100\mathring{A}$ region redward of the Lyα line. We consider only the redward region because the blueward region is affected by IGM absorption. This is only a continuum flux density upper limit because the faint continuum emission level is comparable with the noise in HETDEX spectra. From spectroscopy we measure an average Lyα EW lower limit of $41\mathring{A}$ ranging from $16\mathring{A}$ to $76\mathring{A}$. For Objects 1, 3, 5 we measure a photometric rest-frame Lyα EW compatible with the lower limit from the spectroscopy measure.

In Table 5.3 are reported all the physical parameters that we have presented in this chapter.

Table 5.3: Physical Properties of LAEs

Object	$\Delta v_{\mathrm{Ly}\alpha}$ (km s^{-1})	E(B-V)	$12 + \log(O/H)_{N2}$	SFR^a ($\mathrm{M}_\odot$ yr^{-1})	EW(Lyα)$^b_{rest}$ ($\mathring{A}$)
1	332 ± 21	-0.05 ± 0.10	< 8.44	31 ± 9	87 ± 7 (> 37)
2	287 ± 20	$> 0.$	8.67 ± 0.09	> 34	55 ± 4 (> 76)
3	365 ± 33	0.05 ± 0.27	< 8.03	62 ± 50	44 ± 4 (> 50)
4	256 ± 26	$> 0.$	< 8.41	> 19	$-$ (> 41)
5	250 ± 17	$> 0.$	< 8.47	> 19	63 ± 5 (> 15)
6	130 ± 19	$-$	$-$	$-$	$-$ (> 17)
8	342 ± 22	0.30 ± 0.28	< 8.51	37 ± 34	$-$ (> 68)
COS4 10347	-4543 ± 45	$-$	$-$	135	$-$
COS4 11363	371 ± 96	$-$	$-$	436	$-$
COS4 12148	123 ± 78	$-$	$-$	92	$-$

[a] SFR for COS4 10347, COS4 11363 and COS4 12148 are from the KMOS^{3D} catalog. The others are measured using Hα luminosity from Kennicutt (1998)
[b] EW$_{phot}$ (EW$_{spec}$), where the first is the rest-frame Lyα EW measured using the continuum flux density from broad-band flux and the second is the rest-frame Lyα EW lower limit measured using only spectroscopic information from HETDEX spectra.

Chapter 6

Relations

6.1 Mass - Metallicity relation

In literature there is the suggestion (S14) for LEAs to lie below the mass-metallicity relation (MZR) for continuum-selected star-forming galaxies at a given redshift. We show our results in Figure 6.1, where we place our and S14 LAEs on the stellar mass − gas-phase metallicity plane. For every LAE the metallicity is calculated using the N2 index calibrated by Pettini & Pagel (2004), as is described in Section 5.4. Only Object 9 has an actual metallicity measurement, for all the other sources the inferred 1σ metallicity upper limit is represented with vertical arrows. Stellar masses from COSMOS2015 catalog are measured assuming a Chabrier IMF and S14 uses a Salpeter IMF in the SED fitting. For consistency with our work, we convert the stellar masses of S14 galaxies for which a Salpeter IMF is assumed to a Chabrier IMF, as is described in Madau & Dickinson (2014) by multiplying by 0.61. We also plot the local MZR (Tremonti et al., 2004) (black dashed line, in orange its 1σ confidence region) and MZR at $z \sim 2.3$ (Erb et al., 2006) (black line). Object 2 is the only target with a metallicity measurement from our and S14 samples. This LAE lies above both the local and the $z \sim 2.3$ MZRs but it is compatible (at a 2σ confidence level) with the local MZR. Its high metallicity, for a galaxy with a stellar mass of $\sim 2 \times 10^8$ $M_\odot$, could be due to an overestimation of the [NII]λ6585.23 flux. We fixed the centroid and the FWHM of this line from the Hα detection, in Figure 3.10b is shown that the amplitude of this emission line is similar to the noise in the same region and it could be overestimated for the noise.
Finkelstein et al. (2011) studied the MZR of Lyα emitting galaxies at $z \sim 0.3$, selected from GALEX spectroscopy, and found that they resided below the MZR for SDSS galaxies at similar redshift. Also S14 observed a trend of LAEs being relatively less metal rich than continuum-selected galaxies. From our observation we can't state anything for galaxies at $M_* < 10^9 M_\odot$. The metallicity upper limit of Object 3 is on the MZR, it has 84% chance of lying below the MZR. Object 1 is of particular interest because its position implies that it is less chemically-enriched by at least a factor of 2 than the typical continuum-selected star forming galaxies at the same redshift and with similar stellar mass. However an HST image of Object 1 in Figure 3.2 shows that this object may consist of more than one components. If the observed Hα and [NII]λ6585.23 lines originate only from one component we are overestimating its stellar mass and this would lead to a misplacenent in the mass-metallicity plane.
A larger sample size, with metallicity measurements, will be required to study the mass-metallicity relation for LAEs at similar redshift of this work.

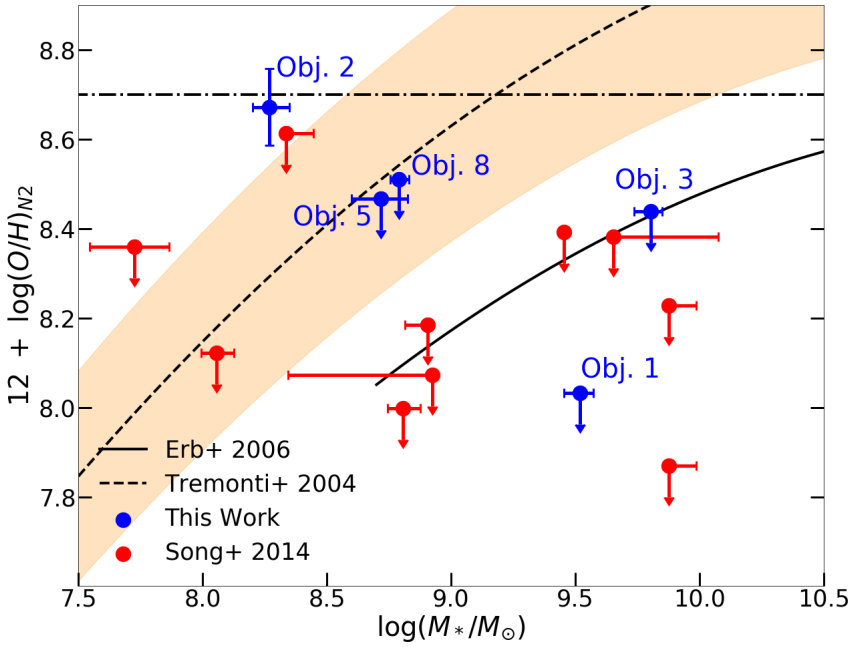

Figure 6.1: A plot of galaxy stellar mass versus gas-phase metallicity. Blue dots are our $z = 2 - 2.5$ LAEs and red dots represent LAEs from S14. Arrows denote 1σ metallicity upper limit. The dashed line represents the $z \sim 0.1$ MZR (Tremonti et al., 2004), in orange its 1σ confidence region. The black line represents the MZR for galaxies at $z \sim 2.3$ from Erb et al. (2006). All points on this figure have their metallicities derived via the N2 index (Pettini & Pagel, 2004). For reference, we denote the solar metallicity by a dash-dotted line.

6.2 Stellar Mass - specific SFR

Using the SFRs we measure from the Hα luminosity in Section 5.6, we investigate the relation between the specific star formation rate, sSFR $\equiv$ SFR/M_*, versus stellar mass for our and S14 samples in Figure 6.2. As noted by S14, massive LAEs have sSFRs similar to those of continuum-selected galaxies at the same redshift and follow the $z \sim 2$ star-forming "main sequence" (Daddi et al., 2007). Low-mass LAEs appear to be undergoing a star-bursting phase with a stellar mass-doubling timescale of as short as a few million years.

LAEs probably are galaxies in a star-bursting phase. Lyα emission correlates with the Hα, the theoretical luminosity ratio is $L_{int}(\text{Ly}\alpha)/L_{int}(\text{H}\alpha) = 8.7$ assuming the Case B recombination, described in Section 5.3. Consequently the Lyα flux correlates with SFR measured from Equation 5.10 and the high sSFR for low-mass LAEs is probably due to the LAEs nature.

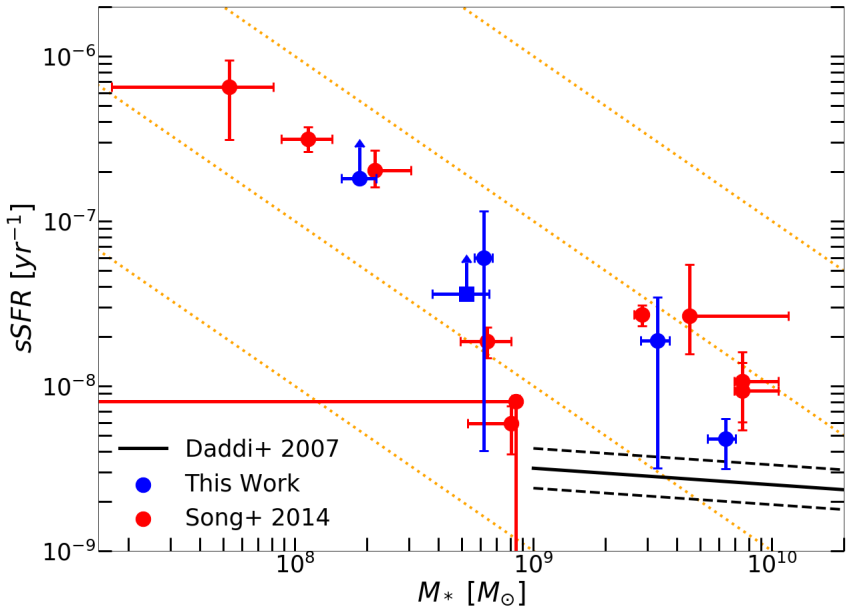

Figure 6.2: A plot of galaxy stellar mass versus sSFR. Blue dots are our $z = 2-2.5$ LAEs and red from S14. The sSFR for our LAEs is measured by using SFR(Hα), the arrow with a dot marker denotes 1σ sSFR lower limit and the arrow with a square marker denotes sSFR lower limit measured assuming E(B-V)=0. The black solid line indicates the $z \sim 2$ star-forming "main sequence" defined by Daddi et al. (2007), the black dashed lines are the interquartile range of 0.32 dex in sSFR. Orange dotted diagonal lines represent constant SFR of 1, 10, 100, 1000 $M_\odot$ yr^{-1} starting from the bottom. All masses are converted to a Chabrier IMF.

6.3 Lyα Velocity Offset vs. Physical Properties

6.3.1 Lyα FWHM - Lyα Velocity Offset

Several works investigate the correlation between the systemic redshift and the Lyα line profile. One of the major studies is Verhamme et al. (2018). Their LAEs sample is composed by 13 sources between $z \approx 3$ and $z \approx 6$ they observed with Multi Unit Spectroscopic Explorer (MUSE) guaranteed time observations and they also use spectroscopic Lyα data from the literature spanning a redshift range from $z \approx 0$ to $z \approx 8$. In this sample they identify two categories of Lyα profiles: spectra with a redshifted single peak and spectra with a double-peaked profile, this last class of LAEs are referred as blue bump LAEs. Firstly they consider only blue bump LAEs, for this objects the systemic redshift always fall between the two Lyα peaks. They find a positive empirical correlation between $\Delta v_{\mathrm{Ly}\alpha}$ (defined as it is shown in Section 5.1) and half of the separation of the peaks ($\Delta v_{1/2}$). The best fit they find is given by:

$$\Delta v_{Ly\alpha} = 1.05(\pm 0.11) \times \Delta v_{1/2} - 12(\pm 37)\ \mathrm{km\ s^{-1}} \tag{6.1}$$

Then they consider the full sample to construct a relation between $\Delta v_{\mathrm{Ly}\alpha}$ and the FWHM of the Lyα red peak. The best-fit between this two parameters is given by:

$$\Delta v_{\mathrm{Ly}\alpha} = 0.9(\pm 0.14) \times FWHM(\mathrm{Ly}\alpha) - 34(\pm 60)\ \mathrm{km\ s^{-1}}. \tag{6.2}$$

This relation is compatible with the one-to-one relation, and its intrinsic scatter estimated from the linear regression is 72 ± 12 km s^{-1}, slightly larger then the intrinsic scatter of the $\Delta v_{1/2}$ method (53 ± 9 km s^{-1}). It is not possible to study Equation 6.1 from HETDEX spectra because VIRUS resolution can not resolve the blue bump. We therefore focus on this last relation. We measure rest-frame FWHM(Lyα) from the Gaussian fit we performed in Section 2.1:

$$FWHM = \frac{2.355 \times \sigma}{1 + z_{sys}}. \tag{6.3}$$

We correct FWHM(Lyα) taking into account the spectral resolution:

$$FWHM[\mathrm{km\ s^{-1}}] = \sqrt{\left(\frac{FWHM}{\lambda_{\mathrm{Ly}\alpha}}\right)^2 - \left(\frac{1}{R}\right)^2} \times c \tag{6.4}$$

where R is the resolving power of VIRUS (R=800 at 450 nm) and c the speed of light. Our data lie systematically under the second relation from Verhamme et al. (2018), as it is shown in Figure 6.3, because it is not possible to resolve the two Lyα peaks in HETDEX spectra. This leads to an overestimation of the FWHM of the redshifted peak and it explains why our data lie below the expected relation.

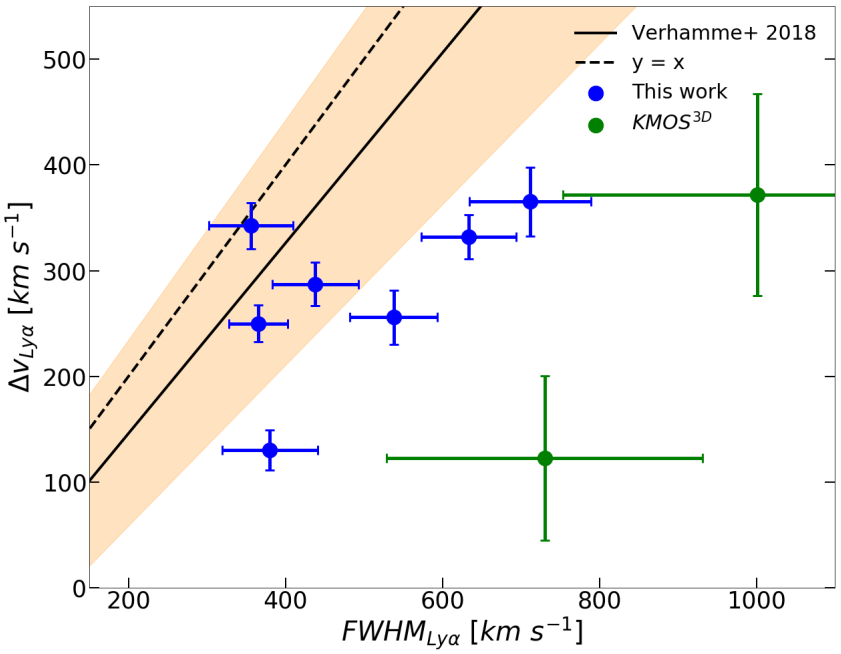

Figure 6.3: A plot of FWHM(Lyα) versus Lyα velocity offset, for the 7 LAEs from this study and 2 from the matching of KMOS^{3D} and HETDEX catalogs. The solid line is the empirical relation proposed by Verhamme et al. 2018 (Equation 6.2) and orange region indicates the 1σ dispersion. The dashed line is the one-to-one relation.

6.3.2 Lyα Velocity Offset vs. Physical Properties

Outflows are believed to be ubiquitous in high-redshift galaxies. This is directly probed by neutral gas in outflows (Martin, 2005) and by studies on metal-line absorption systems along the line of sight of high-redshift galaxies showing metal enriched intergalactic medium, indicating metal must be transported on large scale by galactic outflows (Simcoe, 2006). In observational studies of high-redshift galaxies the outflow is assumed to have a single velocity component, the most discussed scenario is an expanding shell model. This is done for simplicity and due to the limited spectral resolution and SNR available. Although observational studies on local galaxies and theories indicate that outflows are comprised of multiple velocity components. The outflow velocity can be traced directly by UV interstellar absorption lines (Shapley et al., 2003). These are typically observed to be blueshifted by a few hundred km s^{-1} relatively to the systemic velocity in case of outflows. For faint objects as high redshift LAEs, the interstellar absorption lines are extremely difficult to measure since a high SNR continuum is often impractical to obtain. With our data too is impossible to test the presence of a galactic outflow via the interstellar absorption lines. The Lyα line is the only tracer for ISM kinematics. But the main difference is that the Lyα velocity offset is not a direct measure of the outflow velocity. As is described in Chapter 1 simulations from Verhamme et al. (2006) show the main red emission peak measures quite accurately twice the outflow shell velocity for column densities $N_H > 10^{20}$ cm^{-2}: this shift is produced by photons backscattering from the receding side of the expanding shell.
If the Lyα velocity offsets of LAEs are indeed related to outflow velocities, we would expect to see a correlation with other physical properties. In particular where it is assumed that the primary cause of outflows is supernovae winds a correlation is predicted between SFR and outflows (Murray et al., 2011).
As is shown in Figure 6.4 we compare the Lyα velocity offset with the physical properties we extracted in the previous Chapter: the stellar mass (M$_*$), star formation rate (SFR), specific star formation rate (sSFR) and rest-frame Lyα EW (EW$_{\mathrm{Ly}\alpha}$).

Noticeable differences between our LAEs and LAEs from S14 are seen in the top right panel of Figure 6.4, the two samples seem to lie on two different parallel relations. This difference can be explained by considering that SFR in our work and in S14 are both measured from the Hα luminosity, applying Equation 5.10, but we extracted E(B-V) from the Balmer decrement (Equation 5.5) and S14 from a SED fitting. Following the procedure described in Section 5.6 we calculate the SFR(Hα) for the three objects from S14 with a 3σ detection for both Hα and Hβ. In this way we measure an average star formation rate of $\langle SFR_{S14-\mathrm{H}\alpha}\rangle = 38$ M$_\odot$ yr^{-1} for these three LAEs. The average SFR for the same three galaxies from S14 is $\langle SFR_{S14-SED}\rangle = 101$ M$_\odot$ yr^{-1}. We correct the SFR for our LAEs considering the ratio from S14 measures:

$$SFR_{corr} = \frac{\langle SFR_{S14-SED}\rangle}{\langle SFR_{S14-\mathrm{H}\alpha}\rangle} \times SFR_{\mathrm{H}\alpha} = 2.7 \times SFR_{\mathrm{H}\alpha}. \tag{6.5}$$

Upper right panel of Figure 6.4 shows the SFR corrected using Equation 6.5 vs Lyα velocity offset. Considering LAEs from our and S14 sample the Spearman's rank correlation coefficient for SFRs and Lyα offset is $r_s = 0.69$ with a significance of 3σ. This suggests a positive correlation between $\Delta v_{\mathrm{Ly}\alpha}$ and SFR expected for example in an expanding shell model where the outflow is driven by supernovae winds.
The expanding shell model predicts the Lyα equivalent width to correlate positively with the Lyα velocity offset because the outflow velocity aids the escape of Lyα photons. Contrary to what is expected in a expanding shell model in which outflow velocity aids the

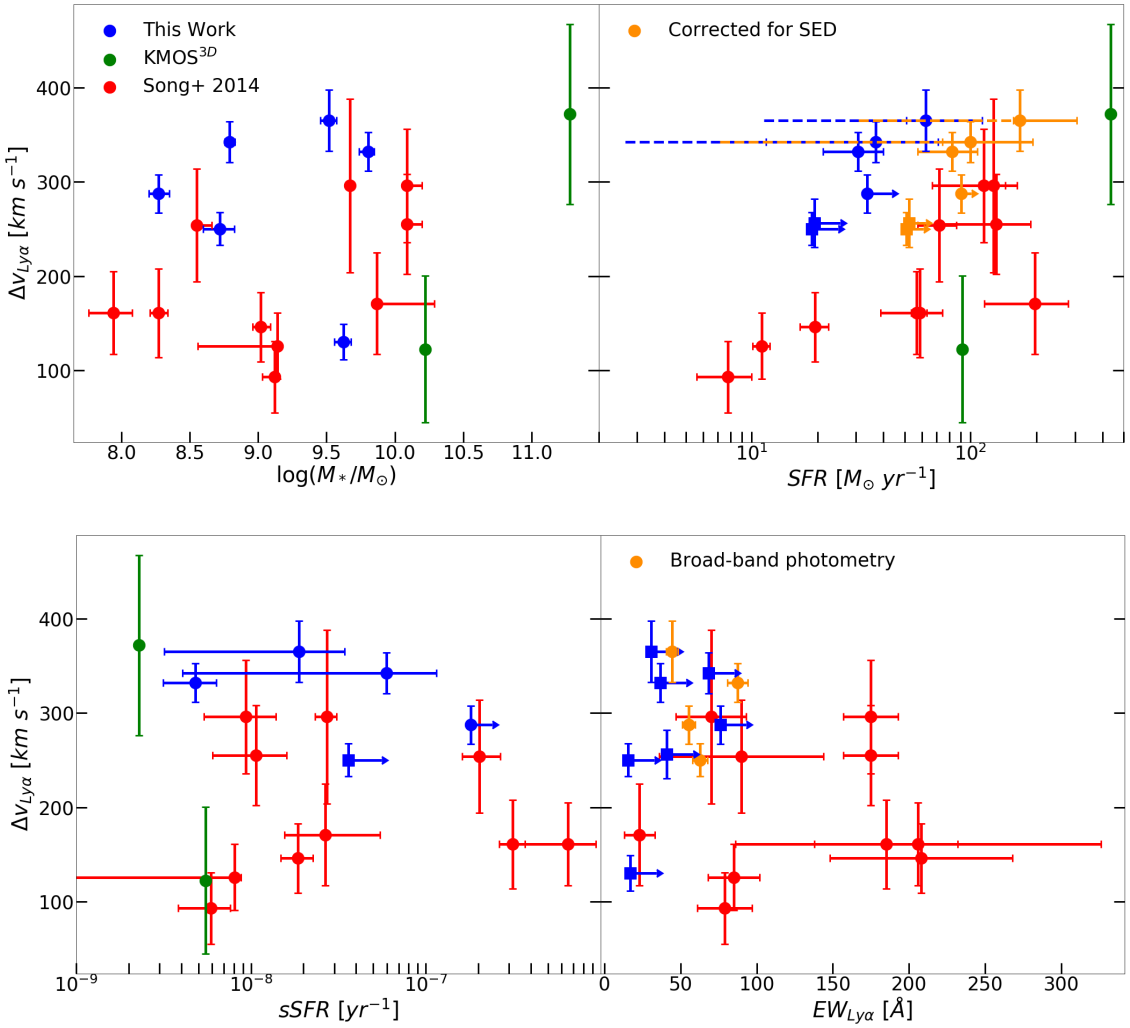

Figure 6.4: Lyα velocity offsets versus varies physical properties. From top left to bottom right, $\Delta v_{\mathrm{Ly}\alpha}$ versus stellar mass, SFR, specific SFR and Lyα rest frame equivalent width. The arrow with a dot marker denotes 1σ lower limit. The arrow with a square marker denotes a lower limit, for these data SFR and sSFR are measured assuming E(B-V)= 0 and for $\mathrm{EW}_{\mathrm{Ly}\alpha}$ are measured using the continuum extracted from HETDEX spectra. In the top right panel dashed lines represent the SFR errors extracted by propagating line flux errors and in orange we plot our SFRs corrected using Equation 6.5. In the bottom line plot blue squares denote Lyα rest frame equivalent width measured from HETDEX data and orange dots denote rest frame $\mathrm{EW}_{\mathrm{Ly}\alpha}$ calculate using broad-band photometry measurements.

escape of Lyα photons, we measure a marginal anti-correlation between $\mathrm{EW}_{\mathrm{Ly}\alpha}$ and $\Delta v_{\mathrm{Ly}\alpha}$ considering the four LAEs from our sample with the $\mathrm{EW}_{\mathrm{Ly}\alpha}$ extracted from the broad-band photometry and LAEs from S14. Hashimoto et al. (2013) found an anti-correlation between Lyα equivalent width and Lyα velocity offset in a compilation of LAE and LBG samples and they conclude that outflows aren't the only mechanism driving the Lyα photons escape. We measure no significant correlation between $\Delta v_{\mathrm{Ly}\alpha}$ and M_* or sSFR.

6.4 The Role of Dust and ISM Geometry on Lyα Escape

Outflows probably aren't the only mechanism driving the escape of Lyα photons. The dust presence and the ISM geometry influence the Lyα photons escape and their contribution has been studied in previous works. In a homogeneous medium where dust and gas are well mixed a negative correlation between the color excess and the Lyα equivalent width is expected. For their resonant nature Lyα photons require many scatters before escaping and consequently have long path lengths in the medium. Therefore the presence of dust can quench Lyα emission and the Lyα flux should decrease with increasing dust content. However S14 and Blanc et al. (2011) find no anti-correlation between Lyα rest-frame equivalent width and color excess. This suggests that the expanding shell is not uniform and that also the geometry of the ISM plays a role in the Lyα escape.
In a clumpy ISM, where dust is confined in the high density regions, Lyα photons would freely travel in the optical thin medium, scatter on high density cloud's surfaces and escape when they don't find any further clump on their path. In this scenario they suffer only little dust extinction. Non resonant photons, as Hα and Hβ which are used to measure the dust content (Section 5.3), penetrate clouds and suffer dust extinction. In this idealized case a positive correlation is expected between Lyα rest-frame equivalent width and dust content. A realistic case is something in between these two cases, where the inter-clump medium is not completely thin. As in S14 we investigate the ISM geometry parameterizing the clumpiness with the parameter q from Finkelstein et al. (2008):

$$q \equiv \frac{\tau_{Ly\alpha}}{\tau_c}, \tag{6.6}$$

where $\tau_{\mathrm{Ly}\alpha}$ and τ_c are the optical depth due to dust respectively for Lyα and continuum photons. The idealized clumpy ISM is described by $q = 0$, the homogeneous medium by $q = \infty$. We study this scenario, as it is conducted in S14, by examining how the ratio of Lyα observed flux to Hα intrinsic flux varies with the dust extinction (E(B-V)). We measure the Lyα escape fraction assuming the Case B recombination, described in Section 5.3 that predicts $L_{int}(\mathrm{Ly}\alpha) = 8.7 L_{int}(\mathrm{H}\alpha)$:

$$f_{esc}(\mathrm{Ly}\alpha) = \frac{L_{obs}(\mathrm{Ly}\alpha)}{L_{int}(\mathrm{Ly}\alpha)} = \frac{L_{obs}(\mathrm{Ly}\alpha)}{8.7 L_{int}(\mathrm{H}\alpha)} = \frac{L_{obs}(\mathrm{Ly}\alpha)}{8.7 L_{obs}(\mathrm{H}\alpha) 10^{0.4 E(B-V) k(\lambda_{\mathrm{H}\alpha})}}. \tag{6.7}$$

The average Lyα escape fraction, for the three LAEs of our sample with $f_{esc}(\mathrm{Ly}\alpha)$ detected, is $\sim 22\%$. It is comparable with the median values of $\sim 19\%$ found by S14 and $\sim 29\%$ found by Blanc et al. (2011).
The E(B-V) uncertainties for our measures are significately larger than those from S14, because we extract the color excess from the Balmer ratio (Section 5.3) and they from a SED fit, and make impossible for us to put any constrain on the impact of the ISM geometry on the Lyα photons escape. For the three galaxies from S14 with Hα and Hβ detected we measure an average color excess error of 0.20, derived from Equation 5.6. This is very similar to the average color error of this work ($\langle \sigma_{EB-V} \rangle = 0.21$).

Chapter 7

Cosmology with LAEs

Galaxy redshift surveys are one of the most powerful tools in modern cosmology. Deducing robust cosmological constraints from galaxy surveys requires an accurate modeling of the observed two-point correlation function and a precise study of possible causes of systematic errors. A galaxy's spectroscopic redshift, as described in Section 1.2, is not given purely by the cosmological expansion. The Universe has inhomogeneities and these induce peculiar velocities in the galaxies. This introduces an extra component to the measured redshifts and gives rise to a difference between the real and the apparent position of a galaxy. This effect is known as redshift space distortions (RSD) and can be used to study the matter distribution producing the distortion.
The HETDEX Survey will use correlation function measurements in the redshift space down to $s \sim 5$ h^{-1} Mpc. This probably requires corrections for Lyα transfer effects down to those scales. How Lyα transfer effects clustering has been studied in Behrens et al. (2018); Byrohl et al. (2019). We can use our measurements of Lyα velocity offsets to add these effects to simulations.

7.1 Correlation function with Lyα velocity offsets

We generate one hundred mock galaxy catalogs in redshift space assuming a log-normal probability density function (PDF) of galaxy and matter density fields using the code described in Agrawal et al. (2017). We draw galaxies by Poisson-sampling the log-normal field. We then calculate the velocity field from the linearised continuity equation of matter fields and we add a contribution from the Lyα velocity offset to the observed redshift as

$$(1 + z_{obs}) = (1 + z_{cos})(1 + z_{pec})(1 + z_{\mathrm{Ly}\alpha}), \tag{7.1}$$

where z_{obs} is the observed redshift, z_{cos} is the cosmological redshift and it is due only to the cosmological expansion, $z_{pec} = v_{\parallel}/c$ is the contribution due to the Doppler effect caused by the component of its peculiar motion along the line of sight direction and $z_{\mathrm{Ly}\alpha} = \Delta v_{\mathrm{Ly}\alpha}/c$ is the correction due to the Lyα velocity offset from the systemic redshift. We add $\Delta v_{\mathrm{Ly}\alpha}$ using a Gaussian distribution with $\langle \Delta v_{\mathrm{Ly}\alpha} \rangle = 273$ km s^{-1} and $\sigma_{\Delta v_{\mathrm{Ly}\alpha}} = 89$ km s^{-1}. These are respectively the average and the standard deviation of Lyα velocity offset for the 9 LAEs from this work (7 from our KMOS observations and 2 from KMOS^{3D} catalog). We add Lyα velocity offsets to the simulations generated as described in Farrow et al. (in prep), see also Leung et al. (2017). A more detailed explanation is given in that paper, but a brief description is given below. We apply angular masks to reproduce the HETDEX field of view shown in Figure 7.1. The fiducial cosmology we use for the simulations is

a flat ΛCDM from Planck 2014 (Planck Collaboration et al., 2014). We add extinction

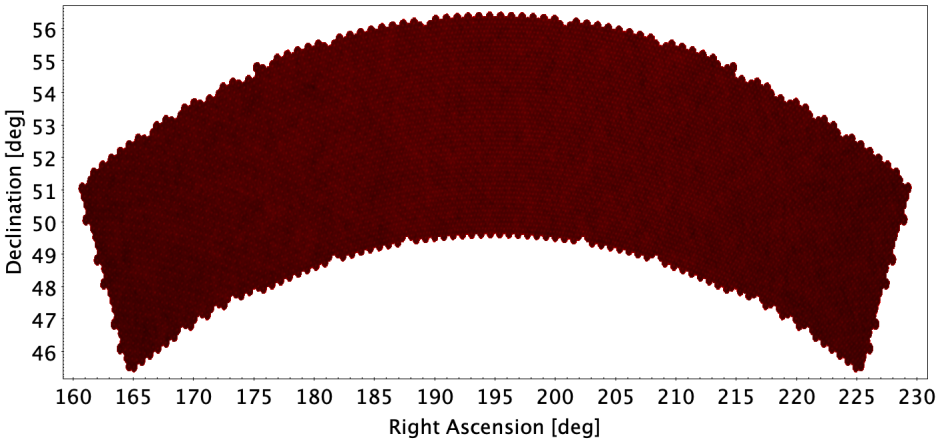

Figure 7.1: A mock catalog of the HETDEX field. The jagged edges are given by the footprint of the 78 IFUs of VIRUS.

to the LAEs using the dustmaps package[1] and the Schlegel, Finkbeiner and Davis (SFD) maps (Schlegel et al., 1998) and using the dust law from Fitzpatrick (1999). We assign fluxes to the LAEs using the luminosity function from Gronwall et al. (in prep). We select the observed LAEs with flux limits based on a Gaussian model of the noise and the 5σ expected flux limit of 5×10^{-17} erg s^{-1} cm^{-2} (Gebhardt et al., in prep). We impose this threshold to every catalog obtaining around half million LAEs each. The distribution of the observed LAEs is shown in Figure 7.2 and the number of observed LAEs in every catalog is comparable to that will be available in the HETDEX Survey.

We measure the correlation function for every mock HETDEX observed catalog using

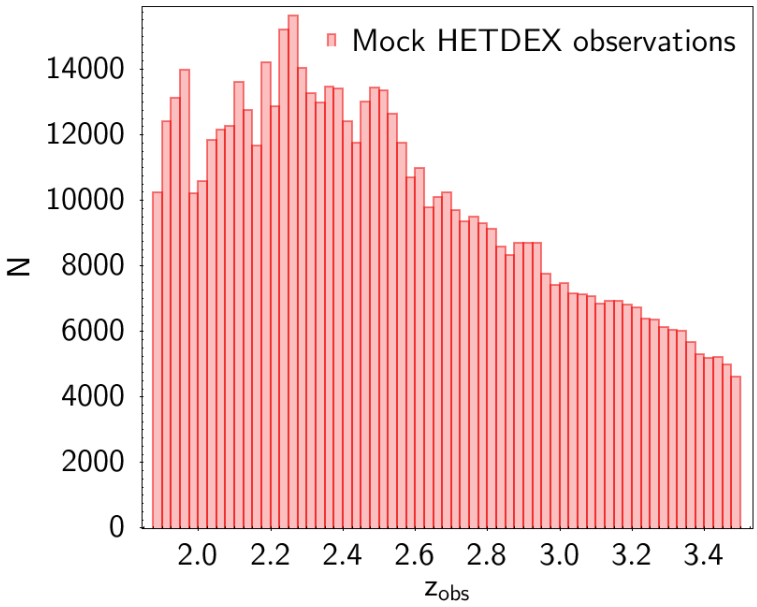

Figure 7.2: Redshift histogram of the mock HETDEX observations.

the estimator from Landy & Szalay (1993) (Equation 1.10) in the redshift space and we

[1]https://dustmaps.readthedocs.io/en/latest/

compute the multipoles $\xi_\ell(s)$ by

$$\xi_\ell(s) = \frac{(1+2\ell)}{2} \int_{-1}^{1} \xi(s,\mu) L_\ell(\mu) \mathrm{d}\mu \tag{7.2}$$

where s is total separation, μ is the cosine of the angle between the separation vector $\mathbf{s}$ and the line of sight direction and $L_\ell(\mu)$ are the Legendre polinomia. In the Figure 7.3 are shown the average multipoles computed from our one hundred mock HETDEX observations and 1500 mock HETDEX observations performed without the Lyα velocity offset. On small scales, $s < 10$ h^{-1} Mpc, the monopole measured from the mock HETDEX observations with the Lyα velocity offset lies below the other (Figure 7.4a) because the additional velocity is Gaussian distributed and it influences the excess probability on small scales.
The distortion caused by the coherent motions of galaxies as they move towards overdense regions, schematically described in Figure 1.2, is known as the Kaiser effect. The quadrupole, $\ell = 2$, of the correlation function is directly bound to this effect. A negative quadrupole corresponds to an apparent flattening of the structure. The Lyα velocity offset counteracts the Kaiser effect, and as is shown in Figure 7.4b reduces the modulus of the quadrupole for $s < 15$ h^{-1} Mpc. The mean Lyα velocity offset artificially pushes all the galaxies to a higher redshift and so distorts their real 3D positions, and the random Lyα velocities blur out structure along the line of sight on small scales and therefore make the observed distribution look more isotropic. This contribution will probably affect the measurement of the logaritmic growth rate $f(z)$, described in Section 1.2, if it is extracted using the correlation function down to $s \sim 5$ h^{-1} Mpc as is planned for HETDEX data. It is not possible to quantify the difference of cosmological parameters in mock HETDEX observations adding the Lyα velocity offset because for now an accurate modeling of the observed two-point correlation function is performed only on scales larger than $s = 20$ h^{-1} Mpc.
Adding the Lyα velocity offset in mock HETDEX observations at $s = 7.5$ h^{-1} Mpc we measure a difference in the correlation function of $0.6\sigma_{\xi_0}$ for $\ell = 0$, of $8.0\sigma_{\xi_2}$ for $\ell = 2$ and of $6.8\sigma_{\xi_4}$ for $\ell = 4$. These correspond to a percentage difference in the correlation function of $\sim 1\%$ for $\ell = 0$, of 13% for $\ell = 2$ and of 35% for $\ell = 4$. The consequences for the derived cosmological parameters are under investigation.

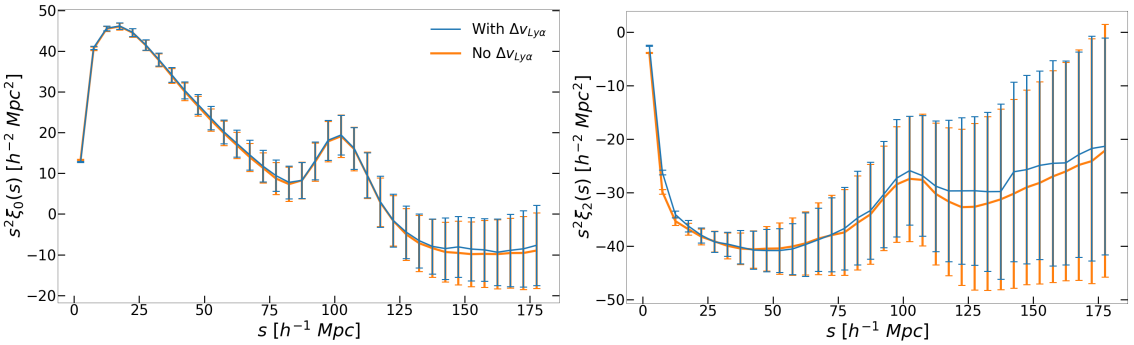

(a) $\ell = 0$ **(b)** $\ell = 2$

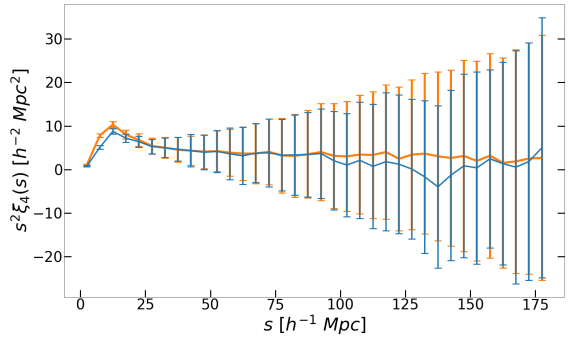

(c) $\ell = 4$

Figure 7.3: The multipoles of the correlation function measured from the mock HETDEX observations. The blue lines show the mean of 100 mock realizations corrected for the Lyα velocity offset, the orange lines show the mean of 1500 mock realizations without the Lyα velocity offset correction. The error bars represent the scatter of the mocks.

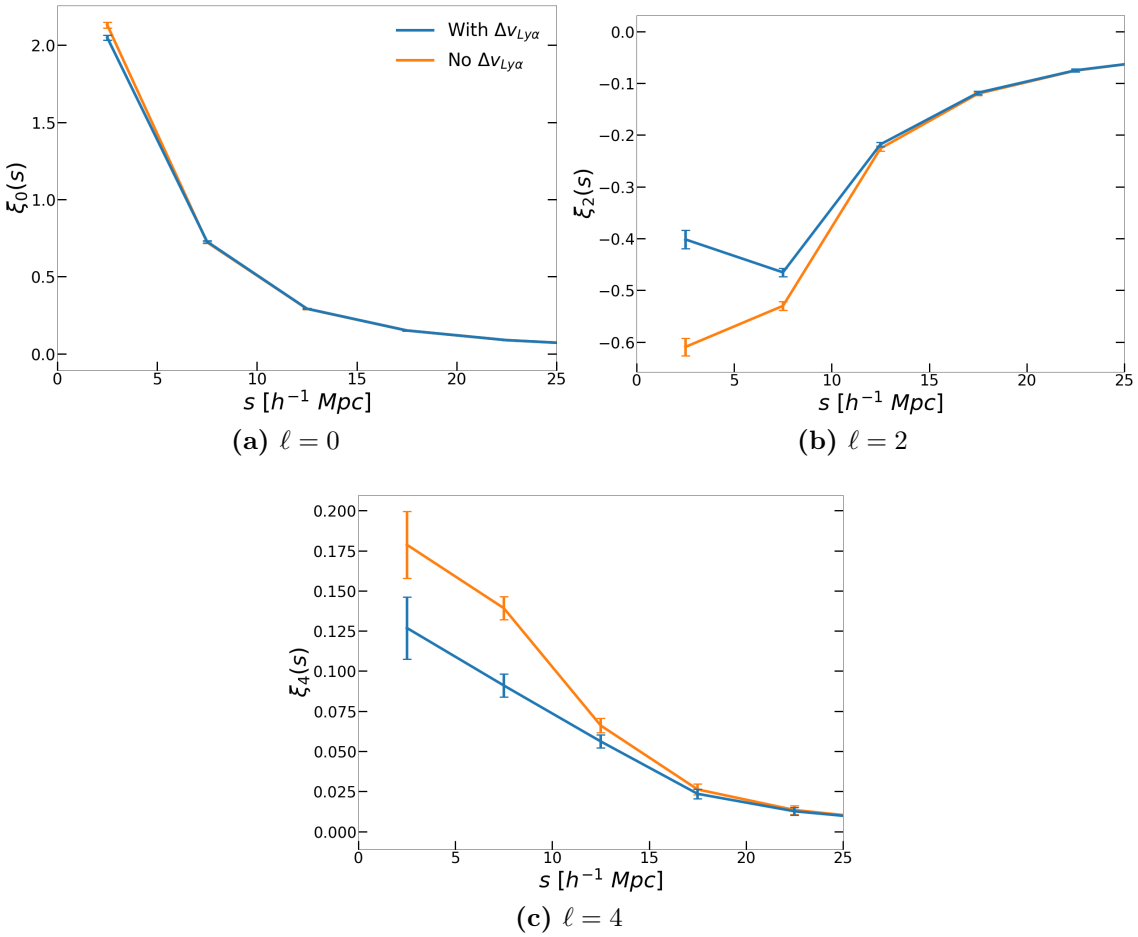

(a) $\ell = 0$ **(b)** $\ell = 2$

(c) $\ell = 4$

Figure 7.4: The multipoles in range $s = 2.5\ \mathrm{h}^{-1}$ Mpc $- 25.0\ \mathrm{h}^{-1}$ Mpc of the correlation function measured from the mock HETDEX observations. The blue lines show the mean of 100 mock realizations corrected for the Lyα velocity offset, the orange lines show the mean of 1500 mock realizations without the Lyα velocity offset correction. The error bars represent the scatter of the mocks.

Chapter 8

Conclusions

We have presented results from VLT/KMOS Near-Infrared spectroscopy for 20 LAEs at $z = 2.1 - 2.5$ discovered from the HETDEX Survey (Hill et al., 2008). Among these 20 LEAs we detected rest-frame optical nebular lines for 8 of them. We add to our analysis three LAEs from the KMOS^{3D} catalog that are present in the first HETDEX data release.

The main results from our analysis combining our near infrared spectroscopic data with Lyα from hdr1 can be summarized as follows:

- We modified the KMOS pipeline to perform optimal sky subtraction and flux calibration in the HK band.
- Among the 20 LAEs observed with KMOS we detected rest-frame optical nebular lines for 8 of them, in particular we detected the [OIII] doublet for 8 LAEs, the Hα emission line for 7 LAEs, the Hβ emission line for 3 LAEs and the [NII]λ6585.23 emission line for 1 LAE. We estimate the Hβ 1σ upper limit for 3 LAEs and the [NII]λ6585.23 1σ upper limit for 5 LAEs.
- We measure the dust reddening $E(B-V)$ from the Balmer decrement, it ranges from $E(B-V) = 0$ to $E(B-V) = 0.30$. We measure the SFR using the relation from Kennicutt (1998) based on the Hα luminosity, the SFR ranges from 19 $M_\odot$ yr^{-1} to 62 $M_\odot$ yr^{-1} with an average of $M_\odot$ yr^{-1}.
- We provide constrains and one measurement on the gas phase metallicities of our sample using the N2 index from Pettini & Pagel (2004) and we study the stellar mass − metallicity realation.
- LAEs appear to be objects undergoing a star-bursting phase, our sample lies above the "main sequence" at $z \sim 2$ in the stellar mass − specific SFR.
- We study the relation between rest-frame Lyα FWHM and Lyα velocity offset from Verhamme et al. (2018). After correcting for instrumental resolution we find a significant deviation from this relation.
- The Lyα line is redshifted respect to the systemic redshift, measured from rest-frame nebular lines, for all LAEs except for one from the KMOS^{3D} catalog. We measure an average Lyα velocity offset of $\langle \Delta v_{\mathrm{Ly}\alpha} \rangle = 233$ km s^{-1} ranging from 123 km s^{-1} to 372 km s^{-1}. This result is comparable with average Lyα velocity offset from Song et al. (2014). We find a moderate correlation of Lyα velocity offset with SFR but no clear correlation with specific SFR, stellar mass and rest frame Lyα equivalent width.

- We measure an average Lyα escape fraction of $\sim 22\%$. It is comparable with the median values of $\sim 19\%$ found by S14 and $\sim 29\%$ found by Blanc et al. (2011).
- We show that correlation function measurements down to $s \sim 5$ h^{-1} Mpc require to take into account Lyα radiative transfer effects. In particular adding the Lyα velocity offset in mock HETDEX observations at $s = 7.5$ h^{-1} Mpc we measure a difference in the correlation function of $0.6\sigma_{\xi_0}$ for $\ell = 0$, of $8.0\sigma_{\xi_2}$ for $\ell = 2$ and of $6.8\sigma_{\xi_4}$ for $\ell = 4$.

Starting from results of this work we plan new near-infrared spectroscopic observation for LAEs selected from the HETDEX survey. In particular in March 2020 we will observe ~ 20 LAEs at $z = 2.1 - 2.5$ in the H and/or K-band with LUCI (LBT Utility Camera in the Infrared), it is a near infrared multi-slit spectrograph at the Large Binocular Telescope (LBT). We are also presenting a proposal to observe rest-frame optical emission lines for a sample of LAEs from the HETDEX survey with MOIRCS (Multi-Object Infrared Camera and Spectrograph) at the Subaru telescope. In this way we will more than double up the number of LAEs observed in the rest frame optical band. With these observations will be possible to study the distribution of Lyα velocity offsets, to study relations between $\Delta v_{\mathrm{Ly}\alpha}$ and different physical properties as metallicity and SFR. We will use these relations to correct the observed redshift for Lyα radiative transfer effects to perform measurements with the correlation function down to $s \sim 5$ h^{-1} Mpc.

Bibliography

Adams, J. J., Blanc, G. A., Hill, G. J., et al., 2011, ApJS, 192, 5

Agrawal, A., Makiya, R., Chiang, C., et al., 2017, JCAP, 10, 003

Baldwin, J. A., Phillips, M. M., & Terlevich, R., 1981, PASP, 93, 5

Behrens, C., Byrohl, C., Saito, S., et al., 2018, A&A, 614, B31

Blanc, G. A., Adams, J. J., Gebhardt, K., et al., 2011, ApJ, 736, 31

Bond, N. A., Gawiser, E., Guaita, L., et al., 2012, ApJ, 753, 95

Bruzual, G., & Charlot, S., 2003, MNRAS, 344, 1000

Byrohl, C., Saito, S., & Behrens, C., 2019, MNRAS, 489, 3472

Calzetti, D., Kinney, A. L., & Storchi-Bergmann, T., 1994, ApJ, 429, 582

Calzetti, D., Armus, L., Bohlin, R. C., et al., 2000, ApJ, 533, 682

Chonis, T. S., Blanc, G. A., Hill, G. J., et al., 2013, ApJ, 775, 99C

Cutri, R. M., Skrutskie, M. F., van Dyk, S., et al., 2003, VizieR Online Data Catalog, 2246

Daddi, E., Dickinson, M., Morrison, G., et al., 2007, ApJ, 670, 156

Davies, R. I., Agudo Berbel, A., Wiezorrek, E., et al., 2013, A&A, 558, A56

Dominguez, A., Siana, B., Henry, A. L., et al., 2013, ApJ, 763, 145D

Erb, D. K., Shapley, A. E., Pettini, M., et al., 2006, ApJ, 644, 813E

Farrow, D. J., et al., 2020, in prep.

Finkelstein, S. L., Rhoads, J. E., Malhotra, S., Grogin, N., & Wang, J., 2008, ApJ, 678, 655

Finkelstein, S. L., Cohen, S. H., Moustakas, J., et al., 2011, ApJ, 733, 117

Fitzpatrick, E. L., 1999, PASP, 111, 63

Gebhardt, K., et al. 2020, in prep.

Good, J. M., Leck, R., Ramsey, J., et al. 2018, procspie, 10700, 107003Y

Gronwall, C., et al., 2020, in prep.

Guaita, L., Acquaviva, V., Padilla, N., et al., 2011, ApJ, 733, 114

Guaita, L., Francke, H., Gawiser, E., et al., 2013, A&, 551, 93

Hansen, M., & Oh, S. P., 2006, MNRAS, 367, 979

Hashimoto, T., Ouchi, M., Shimasaku, K., et al., 2013, ApJ, 765, 70

Herenz, E. C., Urrutia, T., Wisotzki, L., et al., 2017, A&A, 606A, 12H

Hill, G. J., Gebhardt, K., Komatsu, E., et al. 2008, ASP Conf. Proc., 399, 115

Hill, G. J., 2014, Advanced Optical Technologies. Vol 3, Issue 3, 265

Hill, G. J., Kelz, A., Lee, H., et al. 2018a, procspie, 10702, 107021K

Hill, G. J., Drory, N., Good, J. M., et al. 2018b, procspie, 10700, 107000P

Hill, G. J., et al. 2020, ApJ, in prep.

Hoaglin, D. C., Mosteller, F., & Tukey, J. W., 1983, Understanding robust and exploratory data analysis

Ilbert, O., Arnouts, S., McCracken, J., et al., 2006, A&A, 457, 841

Kauffman, G., Heckman, T. M., Tremonti, C., et al., 2003, MNRAS, 346, 1055

Kelz, A., Jahn, T., Haynes, D., et al. 2014, procspie, 9147, 914775

Kennicutt, Jr., R. C., 1998, ARA&A, 36, 189

Kewley, L. J., Dopita, M. A., Sutherland, R. S., et al., 2001, ApJ, 556, 121

Kewley, L. J., Maier, C., Yabe, K., et al., 2013, ApJ, 774, L10

Laigle, C., McCracken, J., Ilbert, O., et al., 2016, ApJS, 224, 24L

Landy, S. D., & Szalay, A. S., 1993, ApJ, 412, 64

Lee, H., Hill, G. J., Good, J. M., et al., 2016, procspie, 9906, 990646

Lee, H., Hill, G. J., Drory, N., et al., 2018, procspie, 10700, 107002B

Leung, A. S., Acquaviva, V., Gawiser, E., et al., 2017, ApJ, 843, 130

Madau, P., & Dickinson, M., 2014, ARA&A, 52, 415M

Marchesi, S., Civano, F., Salvato, M., et al., 2016, ApJ, 817, 34M

Martin, C. L., 2005, ApJ, 621, 227

McLinden, E. M., Finkelstein, S. L., Rhoads, J. E., et al., 2011, ApJ, 730, 136

Momcheva, I. G., Brammer, G. B., van Dokkum, P. G., et al., 2016, ApJS, 225, 27

Morton, D., ApJ. Suppl., 130, 403

Murray, N., Ménard, B., & Thompson, T. A., 2011, ApJ, 735, 66

Osterbrock, D. E., 1989, Astrophysics of gaseous nebulae and active galactic nuclei, ed. Osterbrock, D. E.

Perryman, M. A. C., Lindegren, L., Kovalevsky, J., et al., 1997, A&A, 323, L49

Pettini, M., & Pagel, B., 2004, MNRAS, 348, 59

Planck Collaboration, et al., 2014, A&A, 571, A16

Ramsey, L. W., Sebring, T. A., & Sneden, C., 1994, procspie, 2199, 31

Ramsey, J., Drory, N., Bryant, R., et al., 2016, procspie, 9913, 991346

Sanchez, A. G., 2020, The formation and evolution of cosmic structures

Schlegel, D. J., Finkbeiner, D. P., & Davis, M., 1998, ApJ, 500, 525

Shapley, A. E., Steidel, C. C., Pettini, M., & Adelberger, K. L., 2003, ApJ, 588, 65

Simcoe, R. A., 2006, ApJ, 653, 977

Song, M., Finkelstein, S. L., Gebhardt, K., et al., 2014, ApJ, 791, 3S

Soto, K. T., Lilly, S. J., Bacon, R., et al., 2016, MNRAS, 458, 3210S

Steidel, C. C., Erb, D. K., Shapley, A. E., et al., 2010, ApJ, 717, 289

Storey, P. J., Zeippen, C. J., 2000, MNRAS, 312, 813

Trainor, R. F., Strom, A. L., Steidel, C. C., & Rudie, G. C., 2016, ApJ, 832, 171T

Tremonti, C., Heckman, T. M., Kauffman, G., et al., 2004, ApJ, 613, 898T

Vattiat, B. L., Hill, G. J., Lee, H., 2014, procspie, 9147, 91474J

Verhamme, A., Schaerer, D., & Maselli, A., 2006, A&A, 460, 397V

Verhamme, A., Garel, T., Ventou, E., et al., 2018, MNRAS, 478L, 60V

Wisnioski, E., Förster Schreiber, N. M., Fossati, M., et al., 2019, ApJ, 886, 124

Wright, J. T., & Eastman, J. D., 2014, PASP, 126, 838W